Fuel effects on lean blow-out in a realistic gas turbine combustor

Lucas Esclapez [a,e], Peter C. Ma [b], Eric Mayhew [c], Rui Xu [b], Scott Stouffer [d], Tonghun Lee [c], Hai Wang [b], Matthias Ihme [a,b,*]

[a] Center for Turbulence Research, Stanford University, Stanford, CA 94305, USA
[b] Department of Mechanical Engineering, Stanford University, Stanford, CA 94305, USA
[c] University of Illinois at Urbana-Champaign, 1206 West Green Street, Urbana, IL 61801, USA
[d] University of Dayton Research Institute, 300 College Park, Dayton, OH 45469, USA
[e] CERFACS, 42 avenue G. Coriolis, 31 057 Toulouse Cedex 01, France

ARTICLE INFO

ABSTRACT

Towards the implementation of alternative jet fuels in aviation gas turbines, testing in combustor rigs and engines is required to evaluate the fuel performance on combustion stability, relight, and lean blow-out (LBO) characteristics. The objective of this work is to evaluate the effect of different fuel candidates on the operability of gas turbines by comparing a conventional petroleum-based fuel with two other alternative fuel candidates. A comparative study of fuel properties is first conducted to identify physico-chemical processes that are affected by these fuels. Subsequently, large-eddy simulations (LES) are performed to examine the performance of these fuels on the stable condition close to blow-out in a referee gas turbine combustor. LES results are compared to available experimental data to assess their capabilities in reproducing observed fuel effects. It is shown that the simulations correctly predict the spray main characteristics as well as the flame position. The change in OH^*-emissions for different fuel candidates is also qualitatively captured. An analysis of the flame anchoring mechanisms highlights the fuel effects on the flame position. Finally, the LBO-behavior is examined in order to evaluate the LBO-limit in terms of equivalence ratio and identify fuel effects on the blow-out behavior.

1. Introduction

Increasing concerns about air quality and the need for stable and diverse supplies of jet fuels have motivated significant research efforts on the development and certification of alternative jet fuels for aviation [1–3]. These efforts have been supported through national research programs [4–6] that enable collaborations between universities, governmental research agencies and engine manufacturers. The development of alternatives to conventional petroleum-derived aviation fuels is strongly constrained by the life cycle of commercial jet engines, the compatibility with the present supply infrastructure and the wide range of operating conditions over which safe and reliable combustion must be guaranteed [3]. Consequently, research efforts for the near-term solution have focused on the development of so-called drop-in fuels, which are readily usable as blends in the existing fleet [7]. The certification of alternative fuels through the ASTM D4054 standard [8] requires ex-

perimental test campaigns by engine manufacturers. The objective of these tests is to evaluate the influence of alternative fuel candidates for three key engine operability indicators: lean blow-out (LBO), cold start and high-altitude relight. However, the lack of the predictability of effects of physico-chemical properties of these candidate fuels on turbulent combustion processes results in expensive and long test campaigns. The development of computational fluid dynamics (CFD) tools to better understand these fuel effects in realistic configurations is thus crucial in complementing experiments and reducing cost and duration of the certification process of alternative jet fuels.

The LBO-performance is of primary concern due to the recent emphasis on lean-combustion strategies for emission reduction. Most of the early investigations on LBO focused on bluff-body flameholder configurations [9–11]. Due to limited optical access and absence of high-speed imaging techniques, experiments were used to support the development of semi-empirical correlations to relate LBO-criteria to equivalence ratio and other operating conditions. These correlations were based on three main theories for flame blow-out: (i) extinction of the recirculation bubble, which behaves as a well-stirred reactor [12], (ii) failure to ignite the incoming reactants in the shear layer of the recirculation bubble

* Corresponding author at: Department of Mechanical Engineering, Stanford University, Stanford, CA 94305, USA.

E-mail addresses: esclapez@cerfacs.fr (L. Esclapez), mihme@stanford.edu (M. Ihme).

Nomenclature

χ	scalar dissipation rate
Δh_c	heat of combustion
γ_{LBO}	fuel/air ratio at LBO relative to that of Cat-A2
μ_l	liquid viscosity
ϕ	equivalence ratio
ρ_l	liquid density
σ_l	liquid surface tension
τ_{res}	residence time in the primary zone
We_d	droplet Weber number
P	pressure
T	temperature
$\widetilde{\dot{\omega}}_C$	filtered reaction progress variable production rate
$\widetilde{C}$	filtered reaction progress variable
$\widetilde{Z''^2}$	filtered mixture fraction variance
$\widetilde{Z}$	filtered mixture fraction
d	droplet diameter
q	fuel/air ratio
DCN	derived cetane number
FPV	flamelet/progress-variable
IRZ	inner recirculation zone
LBO	lean blow-out
LFL	lower flammability limit
LHV	latent heat of evaporation
NJFCP	National Jet Fuel Combustion Program
PDPA	phase-Doppler particle analyzer
PVC	precessing vortex core
PZ	primary zone
RR	Rosin–Rammler
SGS	subgrid-scale
SMD	Sauter mean diameter

[13] and (iii) local flame extinction by aerodynamic effects [14]. The review by Shanbhogue et al. [15] describes the blow-off mechanism as a two-stage stochastic process: as the overall equivalence ratio approaches the LBO-limit, the occurrence of local flame extinction increases and close to blow-off the flame behavior is mainly dominated by auto-ignition with successive extinction and re-ignition of the recirculation bubble. Studies of flame stability in swirl-stabilized burners, relevant for modern aviation combustor designs, are more recent and limited. Similar to bluff-body configurations, early work focused on the development of correlations to predict flame stability limits [16]. Compared to simple bluff-body flames, swirl was found to have a beneficial effect on the flame stability [17]. Ateshkadi et al. [18] studied the flame stability in a more complex swirl-stabilized spray combustor and extended the correlation initially proposed by Plee and Mellor [10]. This study indicated that for low gas temperatures, the flame stabilization is controlled by the liquid evaporation rate while at elevated temperatures mixing between fuel and oxidizer is the controlling stabilization process. The effect of liquid fuel was further highlighted by studies in canonical swirling burners [19,20] comparing the LBO-behavior of gas and liquid fueled combustors. Several studies were performed to quantify effects of fuel properties on the LBO-limit in model combustors [16,21–23]. These studies indicate the beneficial effect of lowering the flash point and the adverse effect of an increase in viscosity on the LBO-performance.

Further understanding of the transient blow-out process has only been rendered possible recently by advances in high-speed imaging. Muruganandam and Seitzman [24,25] used high-speed OH*-chemiluminescence imaging to investigate the behavior of a swirled premixed burner close to blow-off. The flame blow-off was found to have several precursor events in which cold gases

were captured by the recirculation zone, resulting in a reduction of the heat release and a change in the flame shape. Using simultaneous high-speed stereo-PIV and OH-PLIF measurements, Stöhr et al. [26] showed that the LBO-behavior in swirled combustors is closely related to the temperature of the recirculation zone and the flame root dynamics; flame extinction was found to occur when the flame root was extinguished by its interaction with the precessing vortex core (PVC) for a duration that exceeds a PVC period. Measurements of the heat release in a swirled bluff-body premixed burner close to blow-off [27,28] and during blow-off [29] revealed that local extinction of the flame in the most intense turbulence regions and entrainment of fresh reactants from the downstream end of the recirculation region progressively reduce the capability of the recirculated flow to ignite the incoming reactants, eventually leading to complete extinction behavior.

Due to the intrinsic transient nature of the LBO-process, comparatively few attempts have been made to evaluate the blow-out behavior through numerical simulations. Such simulations have now become possible using large-eddy simulations (LES) and only recent advances in combustion modeling and computational resources have enabled the computation of transient processes in complex configurations [30,31]. LES of blow-out in the swirl-stabilized spray flame of Cavaliere et al. [20] was performed by Tyliszczak et al. [32] using the LES-CMC model. Blow-out was triggered by a sudden increase in the air mass flow rate and LES was shown to be able to capture the local flame extinction and the subsequent blow-out process. Global extinction in a non-premixed swirl-stabilized burner [20] was studied using the LES-CMC model [33]. The ability of LES to reproduce the experimental blow-off curve was evaluated by performing multiple simulations at different loading parameters. LES was found to predict blow-off limits in terms of air mass flow rate with a 25% accuracy and to reproduce the experimental trends in terms of blow-off duration. The detailed study of the flame front behavior during blow-off revealed that progressive extinction of the flame front on the stoichiometric iso-surface eventually lead to complete flame extinction.

The objective of the present work is to evaluate the capability of LES-methods to describe the sensitivity of LBO to fuel properties in a well-controlled but realistic combustor rig. To this end, a conventional petroleum-derived Jet-A fuel and two alternative fuel candidates are considered. Following the description of the experimental configuration (Section 2) and numerical setups (Section 3), the study consists of three parts:

- Section 4 presents an *a-priori* analysis of the effects of fuel properties on the physical and chemical processes: evaporation and ignition in canonical 0D and 1D configurations.
- Section 5 examines fuel effects on flame stabilization at stable conditions close to blow-out and presents comparisons of LES-results to available experimental measurements.
- Section 6 investigates the transient LBO-behavior through dynamic response simulations. In contrast to previous LES studies, LBO is triggered by reducing the injected fuel flow rate.

The paper finishes with conclusions.

2. Experimental configuration

2.1. Referee combustor rig

The combustor is designed to reproduce important features of a realistic gas turbine combustion chamber in terms of injection system design and air flow staging. A picture of the referee combustor is shown in Fig. 1 and geometric details of the combustion chamber are provided in Fig. 2. The injection system consists of two outer axial swirlers and an inner radial swirler with a pressure-swirl atomizer nested in the center. The atomizer
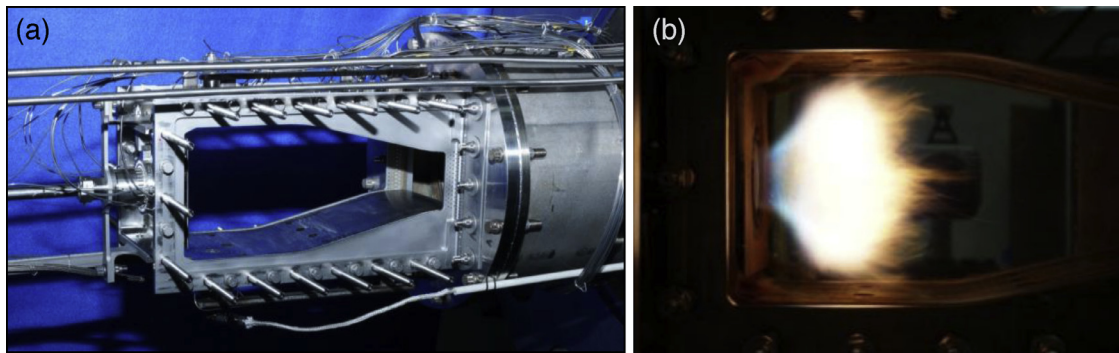
Fig. 1. (a) Disassembled referee-rig combustor. (b) Direct JP-8 flame visualization at 2.07 bar and an overall equivalence ratio of $\phi = 0.1$.
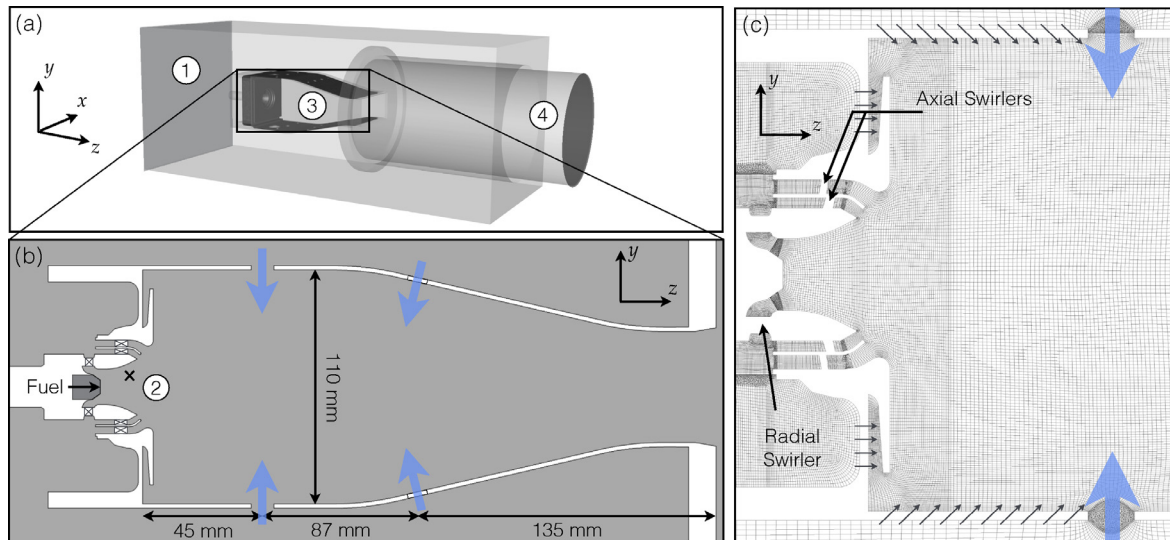

Fig. 2. (color online) (a) Schematic of the computational domain with the main components: 1. Pressurized plenum, 2. Injection system, 3. Combustion chamber, 4. Outlet plenum. (b) Details of the combustion chamber design. Arrows indicates the position of the two rows of dilution jets. (c) Mesh in a central x-normal plane, zoomed on the primary zone.

and the radial swirler are located upstream of the exit plane of the axial swirlers. The injector is mounted in a 110 mm square chamber, and the combustor width is progressively reduced until the exhaust section. A thermal shield is added to protect the liner at the dome of the burner. The combustor walls consist of multi-perforated plates. Dilution holes are located at two axial positions downstream of the injection plane: three holes are located on both the upper and the lower sides of the combustor in a first row 45 mm downstream; a second row, consisting of four dilution holes on each side, is located in the downstream section of the combustor. The combustor is fed by a plenum, and housed inside a pressure vessel with visual access for optical diagnostics of the flame. In the present study, the combustor is fed with air at 394 ± 2.5 K and a relative pressure drop of 3.0% ($\pm$ 0.11% of the vessel pressure) across the injector. The pressure in the combustion chamber is 2.07 ± 0.01 atm and the total air mass flow rate is 391.4 ± 6.9 g/s. The combustor is operated at stable conditions close to blow-off, where the fuel is fully supplied through the pressure-swirl atomizer, at an overall equivalence ratio of $\phi_g = 0.096$ with an uncertainty of 0.15% on the fuel mass flowrate. The fuel is injected at 322 ± 2.3 K with the temperature controlled by a liquid/liquid heat exchanger. Note that the uncertainties provided for the operating parameters include both the uncertainty on the measurements and the spread in holding the values of each parameter from test to test. The characteristic residence time τ_{res} in the primary zone of the combustor (upstream of the first dilution row) is estimated at 5 ms based on the measured flow

rate entering and the volume of the primary zone. Two sets of dual syringe pumps are used to supply and adjust the fuel flow to the rig. The flow rates of fuel and air supplied to the rig are measured with Coriolis meters. The combustor pressure is controlled by using two back pressure control valves operating in parallel.

2.2. Diagnostics

The referee rig was instrumented to provide measurements for pressure, pressure drop, wall temperature, and phase-Doppler particle analyzer (PDPA). The mass flow split measurements were determined using a flow stand specifically built to enable measurements of mass flow through a given section of hardware, while also measuring the pressure, pressure drop and temperature. The mass flow splits were determined by first blocking off all sections of the combustor except the area of interest and then solving for the effective area of the combustor section from measurements of pressure, pressure drop and temperature, and mass flow. Experiments in the flow stand were conducted at room temperature, and atmospheric supply pressure. The pressure drop across the dome (3% of the absolute supply pressure) was the same as that for the combustor experiments. The component areas were then used with the facility measurements of ΔP to determine the relative mass flows for the various sections of the combustor. At stable operating conditions, simultaneous OH^*-chemiluminescence and shadowgraphs were recorded at 10 kHz framing rates, orthogonal to the flow direction. Chemiluminescence was captured using

an intensified camera (LaVision high speed IRO and Photron SA-5) fitted with a Cerco 100 mm, f/2.8 UV lens. The OH*-emissions were isolated using a Semrock Brightline bandpass filter centered around 320 nm with a full width half max (FWHM) of 40 nm and an average transmission of 70% in this wavelength range. The array size was set to 768 × 640 pixels to achieve 10 kHz framing rates. Pixel size calibration was conducted by measuring the height of the plate near the entrance plane of the rig at the centerline, yielding a resolution of 0.165 mm per pixel. At each run condition, the flame was stabilized, and 1000 images were recorded to obtain converged statistical results for comparison with simulations.

In order to evaluate the LBO-limit in a controlled and repeatable manner the following procedure was followed:

- The mass flow used was determined by finding the correct air mass flow to produce the desired dome air pressure drop, and combustor pressure at the desired supply temperature.
- The combustor was lit and the fuel equivalence ratio rapidly adjusted to a level approximately 10% higher than LBO (established by first measuring LBO for a given fuel).
- At this constant equivalence ratio the fuel temperature and the back pressure were adjusted to the appropriate levels. The air mass flow, pressures, and temperatures were set at constant levels.
- The fuel flow rate was then decreased by using the syringe pumps to decrease the fuel flow rate by 1.6 mg/s^2. While the fuel flow was decreased we also maintained the fuel temperature and back pressure at constant levels.
- LBO was assessed by the rapid drop of the signal from a photodiode pointed at the combustor. This threshold crossing of the photodiode was later used to determine the point of LBO. The time required to ramp the fuel down to LBO in the experiments was roughly 240 s. The experiment was then repeated multiple times for a given fuel and test conditions.

For the LBO-limit values presented in this study, the experiment was repeated 84, 15 and 45 times for Cat-A2, Cat-C5 and Cat-C1, respectively.

3. Numerical methods

Figure 2(a) shows the computational domain, which consists of the full experimental pressurized vessel including the plenum, the combustion chamber and the outlet plenum. The domain is discretized using 20 million control volumes with regular hexahedral elements inside the combustor, and tetrahedral elements are used to represent a portion of the injector geometry (Fig. 2(c)). The characteristic mesh size ranges from 0.15 mm in the swirler passages to 0.9 mm in the downstream part of the combustor. Numerical simulations are performed with the low-Mach LES-solver VIDA [34,35]. The instantaneous Favre-averaged conservation equations for mass and momentum are solved on the LES grid with a second-order accurate spacial discretization scheme on unstructured meshes. A second-order predictor-corrector scheme is used for temporal integration. Turbulent subgrid stresses are modeled with the eddy-viscosity model WALE [36]. Walls are considered non-slip and the effusive cooling is modeled through a homogeneous approach, in which the effusive gas-phase velocity is determined from the experimentally measured mass flow rates. Since the flames considered in this study are lifted and the walls of the combustor consist of multiperforated plates, convective heat transfer to the walls is expected to have a limited effect on the flame, so that adiabatic wall boundary conditions are used in the simulations.

Combustion is modeled with the flamelet/progress-variable (FPV) approach [37,38] in which the thermochemical properties are parameterized as a function of filtered mixture fraction $\widetilde{Z}$, filtered reaction progress variable $\widetilde{C}$ and the mixture fraction variance $\widetilde{Z''^2} = \widetilde{Q} - \widetilde{Z}^2$. The governing equations for the combustion model have the following form:

$$\frac{\partial(\overline{\rho}\widetilde{Z})}{\partial t} + \frac{\partial(\overline{\rho}\widetilde{u}_j\widetilde{Z})}{\partial x_j} = \frac{\partial}{\partial x_j}\left[\left(\overline{\rho}\widetilde{D} + \frac{\mu_t}{Sc_t}\right)\frac{\partial\widetilde{Z}}{\partial x_j}\right] + \overline{\dot{S}_Z}, \tag{1a}$$

$$\frac{\partial(\overline{\rho}\widetilde{Q})}{\partial t} + \frac{\partial(\overline{\rho}\widetilde{u}_j\widetilde{Q})}{\partial x_j} = \frac{\partial}{\partial x_j}\left[\left(\overline{\rho}\widetilde{D} + \frac{\mu_t}{Sc_t}\right)\frac{\partial\widetilde{Q}}{\partial x_j}\right]$$
$$- \left[2\overline{\rho}\widetilde{D}\frac{\partial\widetilde{Z}}{\partial x_j}\frac{\partial\widetilde{Z}}{\partial x_j} + 2\overline{\rho D \frac{\partial Z''}{\partial x_j}\frac{\partial Z''}{\partial x_j}}\right] + \overline{\dot{S}_Q}, \tag{1b}$$

$$\frac{\partial(\overline{\rho}\widetilde{C})}{\partial t} + \frac{\partial(\overline{\rho}\widetilde{u}_j\widetilde{C})}{\partial x_j} = \frac{\partial}{\partial x_j}\left[\left(\overline{\rho}\widetilde{D} + \frac{\mu_t}{Sc_t}\right)\frac{\partial\widetilde{C}}{\partial x_j}\right] + \overline{\rho}\widetilde{\dot{\omega}}_C, \tag{1c}$$

where $\overline{\rho}$ is the gas density, $\widetilde{u}_j$ is the velocity component in the jth direction, $\widetilde{D}$ is the scalar diffusivity, μ_t is the subgrid scale viscosity and Sc_t is the turbulent Schmidt number, which is set to a value of 0.9. The last terms on the right-hand side of Eqs. (1a) and (1b) are the source terms due to evaporation, while the last term in Eq. (1c) is the production rate of progress variable. The progress variable is defined as [39] $C = Y_{CO_2} + Y_{CO} + Y_{H_2O} + Y_{H_2}$. $\dot{S}_Z$ and $\dot{S}_Q$ are the evaporation source terms of the mixture fraction and the second moment of mixture fraction, respectively. Note that the evaporation source term of progress variable is neglected because it is much smaller than $\widetilde{\dot{\omega}}_C$.

The flame structure is obtained from the solution of the steady laminar non-premixed flamelet equations, which are solved along the entire S-shaped curve. Cooling effects due to evaporation of the liquid phase on the flamelet solution are considered by computing an effective gaseous fuel temperature [40] $T_{fuel,g} = T_{fuel,l} - \Delta h_v(T_{evap})/c_l(T_{evap})$, where Δh_v is the latent heat of evaporation and c_l is the specific heat capacity of the liquid fuel. The representation of the combustion using an effective composition variable as proposed by Franzelli et al. [41] has not been considered and is subject of future work.

The spray is described using a Lagrangian approach where the droplet motion is represented by the Basset–Boussinesq–Oseen equation and the evaporation rate is based on equilibrium calculations of isolated droplets [42]. Secondary droplet break-up of Lagrangian particles into smaller drops was found to be important. Indeed, in conditions close to LBO, the liquid injection velocity is low and droplets are strongly accelerated by the high flow velocity issued from the inner radial swirler. The droplet Weber number, We_d, defined as $We_d = \rho_l|u_s|^2d/\sigma_l$ (with ρ_l: liquid density; $|u_s|$: local slip velocity magnitude; d: droplet diameter; σ_l: liquid surface tension), is evaluated from the LES and found to reach values in excess of 40 for the largest droplets. About 6% of the droplets exhibit conditions with $We_d > 12$ for a short period of time but these droplets amount to more than 15% of the liquid mass. Secondary breakup is modeled by a stochastic approach [43] where the radius of the droplets is assumed to be a time-dependent stochastic variable with a given initial-size distribution. The critical Weber number $We_{d,c}$ is set to a numerical value of 6 [44] and the sensitivity to this parameter was evaluated by comparing the droplet distribution downstream of the main break-up region obtained using a value of 12 [45]. The spray was found to be only marginally affected by the change in $We_{d,c}$.

Simulations are performed on the NASA Pleiades supercomputer equipped with Ivy Bridge nodes with 2.8 GHz Intel Xeon E5-2680v2 processors, using up to 2000 core. Computing one millisecond of physical time requires approximately 10,000 CPU hours (CPUh) so that approximately two million CPUh were used to complete the present study.

Table 1
Properties of fuels studied.

	Mol. weight	Composition (mass fraction [%])				
	[kg/kmol]	Aromatics	iso-Paraffins	n-Paraffins	Cycloparaffins	Alkenes
Cat-A2	159	18.66	29.45	20.03	31.86	<0.001
Cat-C5	135	30.68	51.58	17.66	0.08	<0.001
Cat-C1	178	<0.01	99.63	<0.001	0.05	0.32
	H/C	Δh_c [MJ/kg]	DCN	T_{10} [K]	$T_{90}-T_{10}$ [K]	μ_l(322 K) [mPa s]
Cat-A2	1.90	43.1	48.3	450.0	67.8	1.17
Cat-C5	1.93	43.0	39.6	434.7	2.9	0.56
Cat-C1	2.16	43.8	17.1	452.1	45.5	0.98

4. Candidate fuels

4.1. Fuel description

The present study considers three fuels, namely a conventional petroleum-derived Jet-A fuel (Designation: Cat-A2, POSF10325) and two alternative fuel candidates: a candidate fuel with a flat boiling curve (Cat-C5, POSF12345) and a candidate fuel with a low Derived Cetane Number (Cat-C1, POSF11498). Key properties of the three candidate fuels are given in Table 1 in terms of composition, H/C ratio, heat of combustion (Δh_c), derived cetane number (DCN), T_{10} and $T_{90}-T_{10}$ characterizing the range of temperature over which the vaporized fuel liquid fraction varies from 10% to 90% (cf. Fig. 4), and liquid viscosity at 322 K corresponding to the injection temperature in the present configuration. Compared to Cat-A2, Cat-C5 has a lower molecular weight, and contains a higher fraction of aromatics and a smaller fraction of branched-chain iso-paraffins. In contrast, Cat-C1 is entirely composed of C12 and C16 iso-paraffins and has a larger molecular weight. Cat-C5 has a similar H/C ratio and Δh_c, while Cat-C1 has a higher hydrogen content resulting in a somewhat larger Δh_c. The major differences between the fuels arise from the low DCN-value of Cat-C1 (due to the highly branched isoparaffins) and the small ($T_{90}-T_{10}$)-range of Cat-C5 with respect to the other candidate fuels. The thermo-physico-chemical properties and combustion chemistry models for all fuels are obtained from studies conducted in the National Jet Fuel Combustion Program (NJFCP) [5] and implemented in the LES-solver. A complete overview of the physical properties of the fuels is provided in Appendix A.

The combustion chemistry models are developed following a hybrid approach [46], in which fuel pyrolysis is described by seven lumped reaction steps, yielding primary pyrolysis products including H_2, CH_4, C_2H_4, C_3H_6, 1-C_4H_8 (1-butene), i-C_4H_8 (iso-butene), C_6H_6 (benzene) and $C_6H_5CH_3$ (toluene). The rates for these pyrolysis products are obtained from time-history data of shock-tube and flow-reactor studies. A foundational fuel chemistry model (USC Mech. II) [47] is then used to describe the oxidation kinetics of the pyrolysis products. The hybrid models, each comprising 112 species and 790 reactions, capture shock-tube ignition delay times over a wide range of pressure, temperature, equivalence ratio and laminar flame speeds for the fuels considered [46]. The combustion chemistry study shows that, despite drastic compositional differences, the Cat-A2 and Cat-C5 behave very similarly in their pyrolysis product distributions, ignition delay times and laminar flame speeds. The differences between these two candidates, if any, are well below the experimental uncertainties of the fuel-speciation measurements. However, in accordance to the observed change in DCN and, more importantly, the fuel chemical composition, Cat-C1 exhibits different pyrolysis yields with a substantially higher fraction of i-C_4H_8 and a lower fraction of C_2H_4.
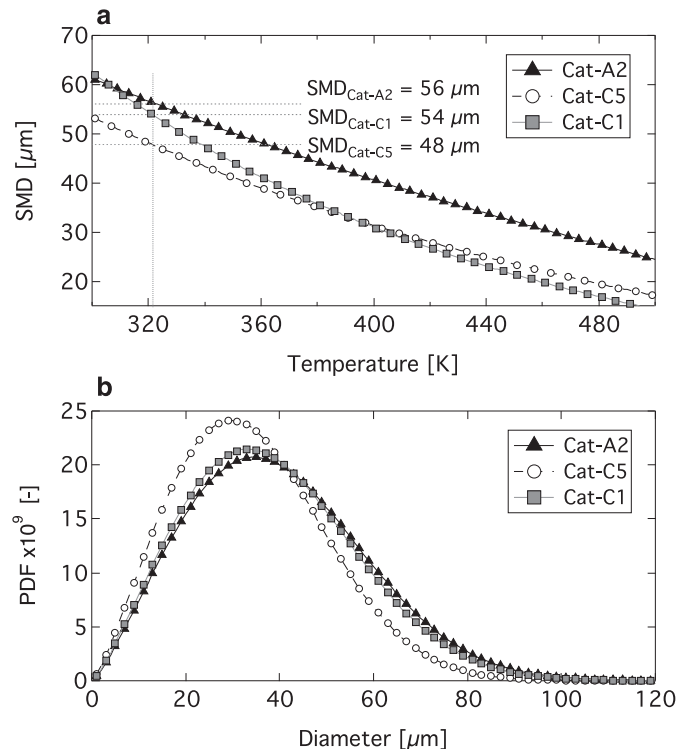
Fig. 3. (a) Effect of temperature on the injection SMD given by correlation of Eq. (2) [45]. (b) Rosin–Rammler droplet-size distribution of Eq. (3) used as spray boundary condition.

4.2. Fuel effect on physico-chemical processes

An analysis is performed to examine effects of fuel properties on droplet evaporation, combustion characteristics and LBO-behavior.

Viscosity and surface tension of the liquid fuel affect the spray preparation during the primary and secondary breakup. To assess the effect of fuel properties on the spray characteristics we use the commonly employed correlation of Lefebvre [45] for the Sauter mean diameter (SMD):

$$d_{SMD} = d_{32} = 2.25\sigma_l^{0.25}\mu^{0.25}\dot{m}_l^{0.25}\Delta P^{-0.5}\rho_{air}^{-0.25},$$
(all quantities in SI-units) (2)

where σ_l is the liquid surface tension, μ_l is the liquid viscosity, $\dot{m}_l$ is the liquid mass flow rate, ΔP is the pressure drop across the injector nozzle and ρ_{air} is the surrounding gas density. The results are provided for all candidate fuels as a function of temperature in Fig. 3(a). The lower viscosity of the Cat-C5 candidate fuel results in a smaller SMD in accordance with experimental observations
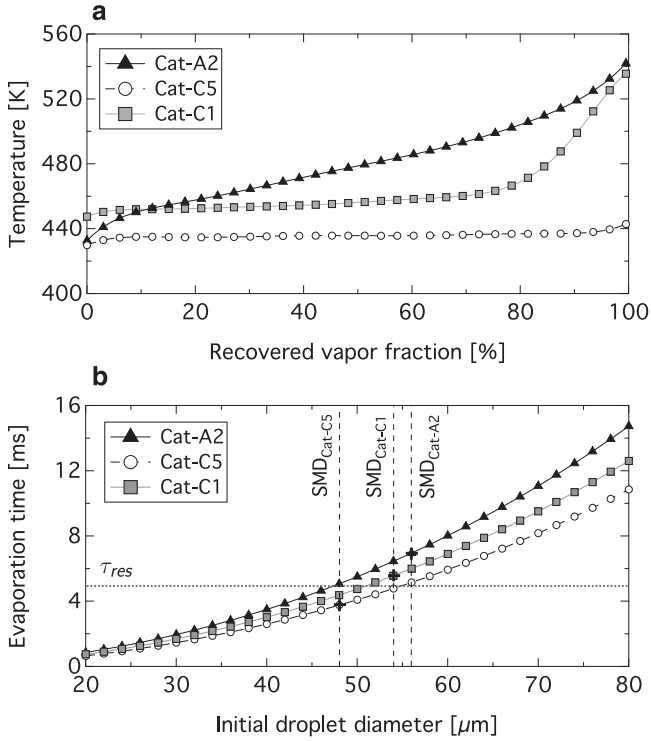
Fig. 4. (a) Distillation curve for all candidate fuels obtained from experiments. (b) Comparison of evaporation time [ms] as a function of initial droplet diameter for all candidate fuels at 2.07 bar and 1000 K.

Fig. 5. (a) Comparison of maximum temperature in counterflow diffusion flame as a function of scalar dissipation rate at 2.07 bar and temperatures of 394 K and 322 K on the fuel side and oxidizer side, respectively. (b) Ignition delay time as a function of temperature, computed for the same conditions with $\phi = 1$.

performed at Purdue [48]. With increasing injection temperature, Cat-C1 progressively diverges from Cat-A2, resulting in a smaller SMD.

Note that the correlation given by Eq. (2) has a functional dependency on the liquid mass flow rate, so that the SMD is updated when reducing the liquid injection during LBO. The SMD from this scaling relation is used to prescribed a Rosin–Rammler (RR) droplet-size distribution as boundary condition for the liquid spray at the vicinity of the injection nozzle. The Rosin–Rammler droplet-size distribution is given as:

$$P(d; \bar{d}, q) = \left(\frac{d}{\bar{d}}\right)^q \frac{q}{d} \exp\left\{-\left(\frac{d}{\bar{d}}\right)^q\right\} \qquad \text{with}$$

$$\bar{d} = d_{SMD} \frac{\Gamma(2/q + 1)}{\Gamma(3/q + 1)}, \tag{3}$$

where the parameter $\bar{d}$ is the characteristic diameter and q is the spread parameter, which is kept constant at a value of $q = 2.25$ [49] for all fuels. The resulting distribution is illustrated in Fig. 3(b). As the droplets are advected downstream, heat-transfer with the surrounding gas phase leads to evaporation. The effect of the fuel properties is evaluated in an isolated 0D droplet evaporation code, where the evaporation time is computed for a range of initial droplet diameters and gas temperatures. Results for an isolated droplet initially at 322 K in an environment at 2.07 atm and 1000 K, corresponding approximately to the equilibrium temperature of the primary zone, are shown in Fig. 4(b). These results show that, compared to Cat-A2, the evaporation rate for Cat-C5 is about 35% faster while the difference is only 16% for Cat-C1. Similar differences are observed for gas temperatures between 700 and 1400 K. These differences can be explained by the change observed on the distillation curves plotted in Fig. 4(a): Cat-C5 has a flat and low temperature curve consistent with its higher aromatic and lighter paraffinic content than Cat-A2, which exhibits a quasi-linear distillation curve that extends over a large tempera-
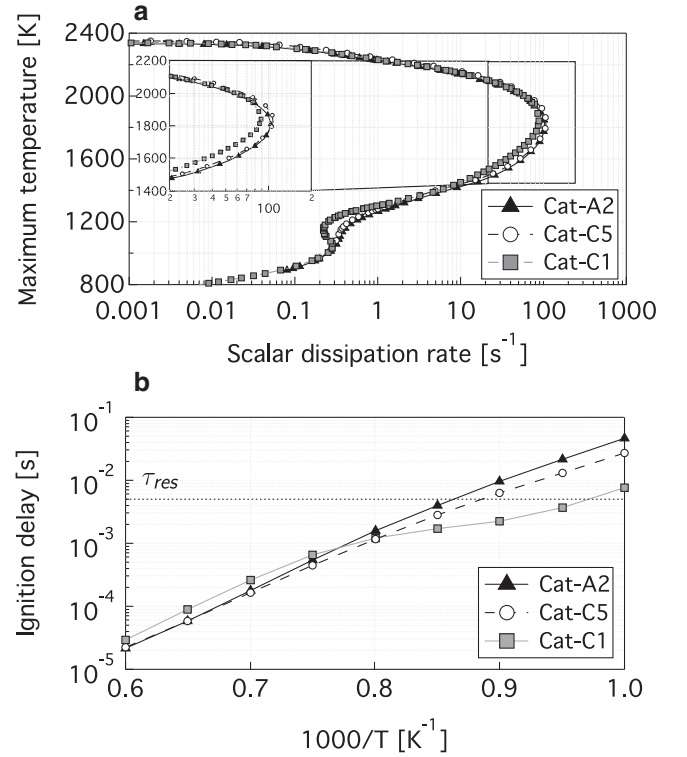
ture range. The horizontal dashed line in Fig. 4(b) shows the characteristic residence time τ_{res} in the primary zone while the vertical dashed lines show the injection SMD for all candidate fuels. The intersection between the vertical dashed line and the evaporation time provides an estimate for the characteristic evaporation time for each fuel candidate. This evaporation time is found to be larger than the residence time in the primary zone for Cat-A2 and Cat-C1 but smaller for Cat-C5, highlighting the effect of fast evaporation on the fuel availability in the primary zone.

The effect of the fuel composition on the combustion chemistry is evaluated by considering a counterflow diffusion flame configuration, which is relevant to the FPV-combustion model adopted in this study. Chemical effects are evaluated by comparing the S-shaped curves for the three fuels as reported in Fig. 5(a). Through this study, only marginal differences for the response to strain are observed between Cat-A2 and Cat-C5, both fuels having an extinction scalar dissipation rate of $\chi_{Z,ext} = 105$ s^{-1}. Small differences are observed between Cat-A2 and Cat-C1 with the extinction rate of the latter around $\chi_{Z,ext} = 88$ s^{-1}. A more distinct difference between the chemistries of Cat-A2 and Cat-C1 is observed from Fig. 5(b), showing the ignition delay time of a homogeneous reactor as a function of temperature. The ignition delay of Cat-C1 is found to be significantly shorter than that of Cat-A2 at low temperature and to be slightly larger at higher temperatures.

To complete the study, the fuel effect on the LBO-limit is evaluated, with respect to the performance of the reference fuel Cat-A2, using the empirical correlation developed by Lefebvre [16]:

$$q_{LBO} \propto \frac{f_{PZ}}{V_{PZ}} \frac{\dot{m}_a}{P_3^{1.3} \exp(T_3/300)} \frac{d_0^2}{\lambda \Delta h_c} \tag{4}$$

where q_{LBO} is the fuel/air ratio at the LBO-limit, f_{PZ} is the fraction of the total airflow entering the primary zone (PZ), V_{PZ} is the volume of the primary combustion zone, $\dot{m}_a$ is the air mass flow rate,

Table 2
Fuel effects on LBO-limit using empirical correlations.

	Cat-C5	Cat-C1
$d_{r, SMD}$	0.86	0.96
d_{r,We_c}	1.02	0.95
λ_r	1.35	1.16
$\Delta h_{c, r}$	1.00	1.02
$T_{crit, r}$	0.98	0.88
$\gamma_{LBO, SMD}$ ($T_{crit, r} = 1$)	0.55	0.78
γ_{LBO,We_c} ($T_{crit, r} = 1$)	0.77	0.76
$\gamma_{LBO, SMD}$	0.54	0.69
γ_{LBO,We_c}	0.76	0.67

P_3 is the inlet pressure and T_3 is the fresh gas temperature, d_0 is the mean drop size, Δh_c is the heat of combustion and λ is the effective evaporation constant. The first and second term on the right-hand side of Eq. (4) represent the effect of the combustor design and operating conditions, respectively. These terms are independent of the fuel properties and are kept constant in the following. The third term embodies fuel effects. Note that Eq. (4) was developed assuming that LBO occurs when the temperature in the primary combustion zone drops below a critical value, assumed to be constant for all candidate fuels. Hence, the chemistry effect is only included through the use of the heat of combustion. Assuming that the flame stabilization is controlled by auto-ignition of the mixture in the primary zone, the critical temperature $T_{crit, PZ}$ can be defined as the temperature at which the auto-ignition time equates the residence time in the primary zone (cf. Fig 5). Eq. (4) can be rewritten as:

$$q_{LBO} \propto \frac{f_{PZ}}{V_{PZ}} \frac{\dot{m}_a}{P_3^{1.3} \exp(T_3/300)} \frac{d_0^2 T_{crit,PZ} \overline{c_p}}{\lambda \Delta h_c} \quad (5)$$

where $\overline{c_p}$ is the heat capacity of gaseous mixture. Since the combustor design and the operating conditions are kept constant in the present study, the LBO-limit only depends on the third term and is given with respect to that of Cat-A2:

$$\gamma_{LBO} = \frac{q_{LBO,f}}{q_{LBO,A2}} = \frac{d_r^2 T_{crit,r}}{\lambda_r \Delta h_{c,r}} \quad (6)$$

where the subscript f is either Cat-C5 or Cat-C1 candidate fuel and the subscript r indicates quantities relative to that of Cat-A2. The mixture heat capacity $\overline{c_p}$ is not affected by the change in fuel. The diameter ratio d_r is evaluated using two characteristic diameter estimates: $d_{r,SMD} = d_{SMD,f}/d_{SMD,A2}$ using Eq. (2) and a second estimation is made using the maximum diameter after secondary break-up given by:

$$d_{We_{d,c}} = \frac{We_{d,c}}{|u_s|^2} \frac{\sigma_l}{\rho_l} \quad (7)$$

where the critical Weber number and the slip velocity magnitude are assumed to be constant when computing $d_{r,We_c} = d_{We_{d,c},f}/d_{We_{d,c},A2}$. The evaporation constant is evaluated as the inverse of the evaporation time reported in Fig. 4 and the heat of combustion are reported in Table 1.

Table 2 summarizes the fuel effect on the LBO-limit compared to the Cat-A2 fuel using the two estimates of the characteristic droplet diameter, and comparing the original formulation of Lefebvre [16] ($T_{crit,r} = 1$) and the one proposed in Eq. (5). The results show that using the original formulation, the LBO-limit is significantly lower for both candidate fuels, mainly due to the change in characteristic droplet diameter and evaporation rate. The difference between the two fuels is reduced when using the characteristic diameter after secondary break-up since the lower surface tension of Cat-C1 induces smaller droplets. When taking into account the effect of the fuel auto-ignition delay, the LBO-limit of Cat-C1

is lowered as a result of its faster auto-ignition at low temperature compared to the other two candidate fuels.

In summary, this analysis indicates that the difference in physico-chemical properties between the reference fuel Cat-A2 and the candidate fuels primarily affects the physical processes and the chemical kinetics for Cat-C5 and Cat-C1, respectively. From empirical correlations, developed from previous combustor designs, a significant effect of the fuel on the LBO-limit can be expected, and the deviation from the conventional fuel (Cat-A2) is related to differences in the physical properties.

5. Stable operating conditions

Stable non-reacting and reacting operating conditions are considered first in order to compare LES-results against experimental data. The flow split and pressure drop obtained from the non-reacting flow simulations are compared to measurements performed on the individual components of the combustion chamber on a separate flowbench. LES results obtained for reacting conditions for all candidate fuels are then compared to chemiluminescence and PDPA measurements, and are further investigated to quantify fuel effects.

5.1. Non-reacting flow simulations

To provide a general assessment of the LES to reproduce the experimental flow conditions, velocity statistics are collected for a non-reacting simulation over four residence times (20 ms). The flow split between the swirler, dilution holes and effusive plate is computed and compared to experimental measurements. Note that measurements are performed on a separate flowbench where the effective area of each component is measured by blocking all others. Simulations performed by Briones [50] showed that this procedure results in differences in the measurement of the effective area of the swirler passages due to pressure coupling between the passages. The results are summarized in Table 3. Two measurements are performed and both the averaged values and the standard deviations (in parenthesis) are presented for each element of the combustor. There are discrepancies in the flow split between inner and outer axial swirlers of the injection system. Besides the uncertainty of the measurement technique, these differences can partially be attributed to the underresolution of the boundary layer in the swirler vanes and the effect of the SGS-model. The sensitivity to the SGS-model was evaluated by comparing the flow split obtained using WALE [36] and Vreman [51] closure models. Results from this study showed that larger differences are obtained with the Vreman model, especially between the inner and outer axial swirler, as a result of the under-estimation of the wall shear stress.

Since the flow split between the swirler and the dilution rows is well predicted in the simulations, the overall equivalence ratio in the primary zone is expected to be well reproduced by the LES. The uncertainty on the flow split between the inner and outer axial swirler can lead to an erroneous momentum distribution right at the exit of each passage. However, both swirlers exit around the same location and their streams are found to rapidly merge downstream, so that the effect of the difference between experiments and simulations is expected to be small near the flame position. Note also that since the entry position of these two components are very close, the flow split measurements are subjected to large uncertainty when blocking one or the other.

5.2. Flame structure and dynamics for stable conditions

Before examining the transient flame behavior during LBO, simulations are performed at steady operating conditions at an overall

Table 3

Comparison of measured (along with experimental relative standard deviation σ) and computed mass flow rates through swirler, effusion plates and dilution holes. Relative differences between experiments and simulations are shown in parentheses.

	Experiments		LES WALE		LES Vreman	
	Average [g/s]	σ [± %]	[g/s]	(% diff)	[g/s]	(% diff)
Swirler radial	13.6	5.1	14.4	(5.9)	14.9	(9.6)
Swirler axial int.	21.0	10.0	18.4	(−12.3)	23.4	(11.4)
Swirler axial ext.	25.3	2.8	28.6	(13.0)	32.3	(27.7)
Swirler cooling	1.7	71.0	–	–	–	–
Total swirler	61.6	1.5	61.4	(−0.3)	70.6	(14.6)
Effusion plates	243.3	0.9	241.1	(−0.9)	241.1	(−0.9)
Dilution row 1	40.3	2.0	42.8	(6.2)	38.5	(−4.5)
Dilution row 2	46.1	1.5	46.1	(0.1)	41.3	(−10.3)

Table 4

Experimental LBO-limit and standard deviation for all candidate fuels along with characteristics for the steady operating conditions.

	Units	Cat-A2	Cat-C5	Cat-C1
$\phi_{LBO,\,exp.}$	[−]	$0.0806 \pm 8.95 \times 10^{-4}$	$0.0825 \pm 9.52 \times 10^{-4}$	$0.0869 \pm 7.60 \times 10^{-4}$
ϕ_g	[−]	0.096	0.096	0.096
ϕ_{PZ}	[−]	0.381	0.381	0.381
$\phi_{swirler}$	[−]	0.614	0.614	0.614
$\phi_g/\phi_{LBO,\,exp.}$	[−]	1.191	1.164	1.105
$\dot{Q}$	[kW]	110.5	110.5	110.0
$\dot{m}_l$	[g/s]	2.563	2.569	2.51
$d_{32,\,inj}$	[μm]	56	48	54

equivalence ratio slightly above the experimentally observed blow-off value. The operating conditions for the steady simulations are listed in Table 4 for all three fuels. Averaged values for LBO-limits and standard deviations calculated over multiple experiments are also reported. Three equivalence ratios are introduced based on the total air flowrate (ϕ_g), the primary zone flowrate (ϕ_{PZ}) and the swirler flowrate ($\phi_{swirler}$), showing the degree of mixing induced by secondary air flows. The primary zone equivalence ratio is calculated using the air flow through the swirler, a quarter of the first dilution jet flowrate and the dome effusive cooling flowrate. The objective of this study is to: (i) assess the LES-results against available experimental data, (ii) analyze the flame stabilization, and (iii) evaluate the fuel effects. Statistical results for gaseous and spray data are collected over four residence times (20 ms) after reaching a statistically stationary state.

5.2.1. Assessment of LES results

Experimental data are available for the operating conditions listed in Table 4, which allows for evaluating the capability of the LES to reproduce experimentally observed trends in terms of spray dispersion and droplet distribution as well as flame position and dynamics. In this context, it is noteworthy to mention that the experimental data were available only after the simulations were performed, so that the present analysis constitutes essentially a blind comparison. Figure 6 shows a comparison of the droplet statistics against PDPA-measurements for all three candidate fuels (rows) in terms of SMD, axial and radial velocity components at three axial positions downstream of the thermal shield. Only locations with a significant number of samples (>1000) are represented for both experiments and LES.

This comparison indicates that the LES is able to adequately reproduce the spray angle and the magnitude of the velocity components. However, the SMD is found to be underestimated from the LES. Experiments show a bi-modal shape of the radial SMD-profile close to the injection system, which is not captured in the LES. This could be the effect of liquid wall filming in the inner passage of the injector, and is currently further investigated experimentally. A closer analysis of the droplet size distribution for Cat-A2 at two ra-

dial positions is presented in Fig. 7. The droplet distribution shows that the most probable droplet diameter d_{mp} is fairly well reproduced by the LES but large droplets are missing. This difference can be related to uncertainties in the critical Weber number, which determines the break-up of large droplets as they accelerate through the shear layer between the inner recirculation zone (IRZ) and the radial swirler flow near the pressure-swirl nozzle. Only marginal differences between the different fuels can be observed from experiments and simulations.

To provide qualitative comparisons of the flame position between experiments and simulations, all chemical mechanisms are augmented by an OH*-kinetic scheme [52] and OH* is included in the flamelet library. Figure 8(a) shows a line-of-sight integrated view of the OH*-emissions for all candidate fuels: the upper part corresponds to LES time-averaged OH* mass fractions while the lower part shows the OH*-emissions from experiments. Experiments and simulations are normalized by the respective maximum OH*-value for the Cat-A2 case. The first observation is that all flames are found to be lifted from the injector. This is also observed from the direct flame visualization presented in Fig. 1(b). The experiments show a strong asymmetry of the OH*-emissions for Cat-A2 which is not observed in the LES. Both experiments and simulations indicate higher OH*-emissions for Cat-C1 with maximum levels located closer to the injector than the other fuels. A more quantitative comparison of the fuel effects is obtained by computing the planar averaged OH*-emissions as a function of the axial distance from the injection system. The results are shown in Fig. 8(b) where both experiments and simulations are normalized by the respective maximum OH*-value of Cat-A2. In accordance with experiments, the simulations predict higher OH*-emissions for Cat-C1 and the flame is sitting closer to the injector, compared to the other two candidate fuels. Emission levels are fairly similar for Cat-A2 and Cat-C5 in both LES and experiments. The location of the mean flame base, defined as the position where normalized OH*-emissions exceed 0.1, is further downstream for Cat-C5 in the experiments, but this behavior is not observed in the LES. This can be explained by the occurrence of combustion dynamics for Cat-C5 away from LBO-conditions ($\phi_g > 0.09$). These instabilities were
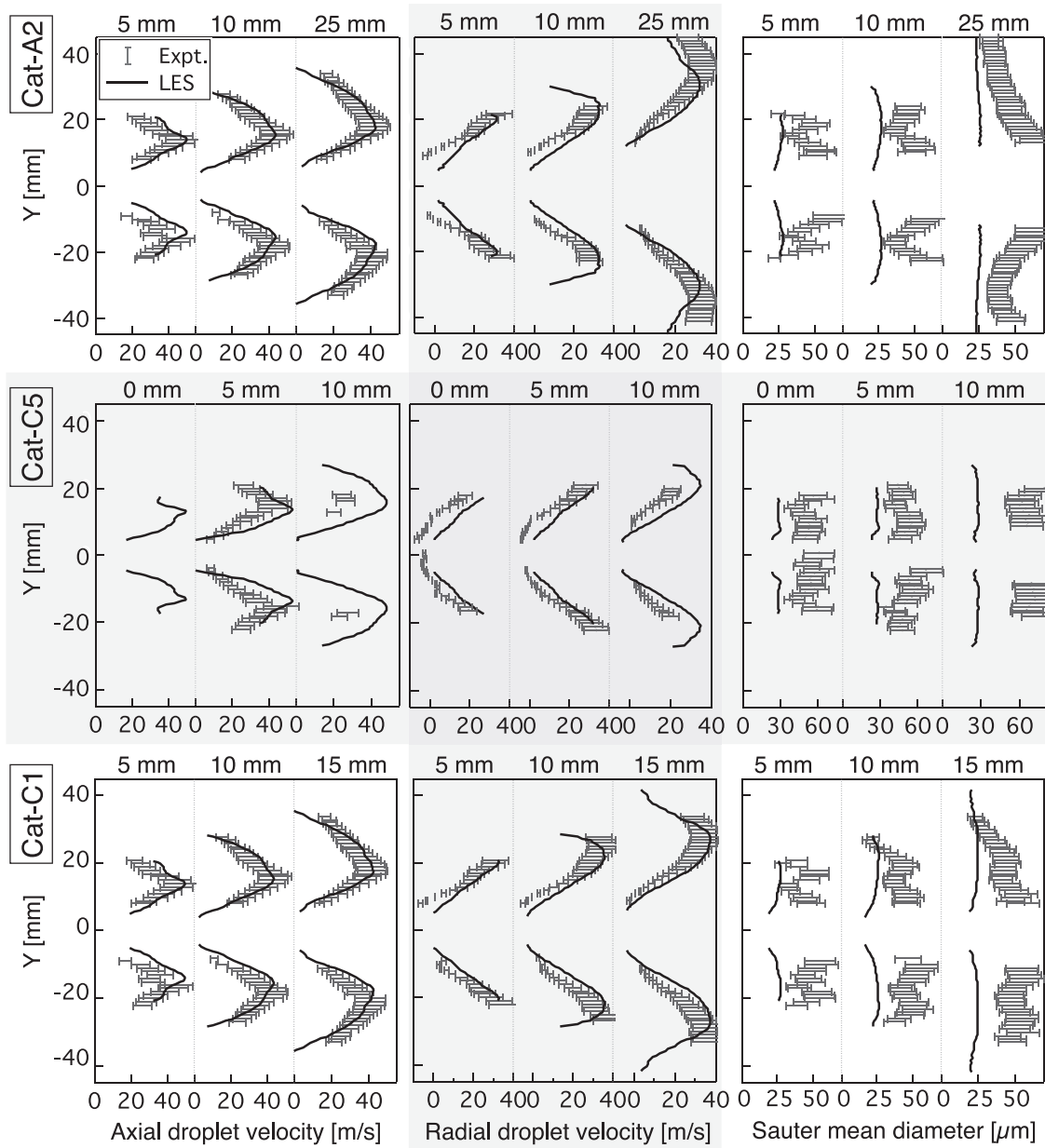
Fig. 6. Comparison of axial droplet velocity, radial droplet velocity and SMD between PDPA and LES at three axial positions in the combustion chamber for all candidate fuels. Error bars indicate experimental uncertainties of 10% of the PDPA measurements (as specified by the manufacturer).

reported after the simulations were performed, and are not considered in the present simulations.

5.2.2. Fuel effects on the flame stabilization and reacting flow statistics

The flow field in the referee combustor rig is representative of rich-burn/quick-quench/lean-burn (RQL) combustor designs, where the strong swirl induced by the injection system generates a large IRZ, which extends upstream within the injector and interacts downstream with the first row of the dilution holes. Figure 9 shows instantaneous iso-surfaces of progress variable source term ($\widetilde{\dot{\omega}}_C = 100$ s^{-1}) colored by temperature to identify the flame position, droplets, and large ($u_y = \pm 80$ m/s) transverse gaseous velocity iso-surfaces highlighting the position of the dilution jets. The flame is found to be confined to the primary zone and to be approximately distributed on an annulus around the swirled jets. The flame front is highly corrugated and interacts with the first

row of dilution jets. Near the pressure-swirl injector nozzle, the spray interacts with the IRZ and due to the low liquid momentum, droplets are deflected toward the fresh-gas stream of the inner radial swirler. The pre-heat temperature of the incoming air is below the T_{10}-temperature (cf. Table 1) for all three candidate fuels. Thus, low evaporation rates are observed before the droplets encounter hot recirculated gases. The IRZ advects hot gases toward the injection nozzle acting as a flame stabilization mechanism. However, the combined effects of the low IRZ temperature due to the low equivalence ratio and the rapid mixing induced by the high velocity within the injection system, strongly reduce the heat transfer between gas and liquid. The flame is then lifted, with only rare occurrences of chemical reaction at the upstream tip of the IRZ.

Time-averaged fields for temperature and progress variable source term are shown in Fig. 10 in central x-normal (left) and y-normal (right) cut planes for all fuels. Velocity streamlines are superimposed on the temperature field to highlight the
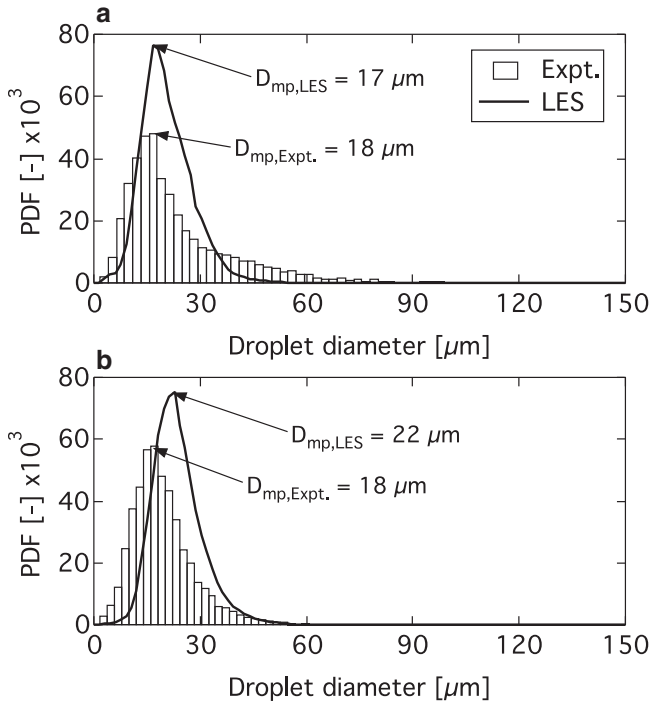
Fig. 7. Comparison of droplet size distribution between simulations and experiments for Cat-A2 at 5 mm downstream of the deflector plate: (a) radial position: 10 mm. (b) radial position: 15 mm.
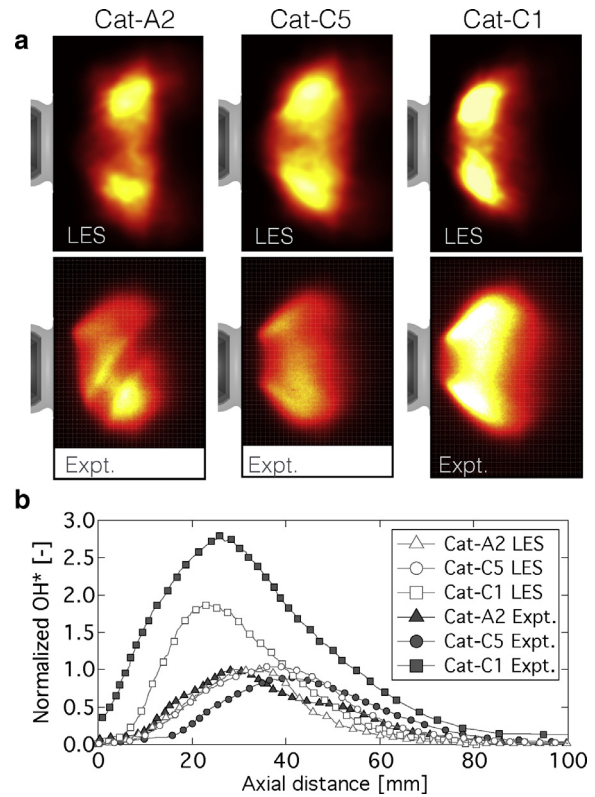

Fig. 8. (color online) (a) Line-of-sight integrated normalized OH*-emissions at $\phi_g = 0.096$. Top: OH* mass fraction from LES, bottom: experiment chemiluminescence. (b) Comparison of plane-averaged OH*-emission against experimental data for all candidate fuels.

recirculation zones while iso-contours of the evaporation source term of mixture fraction are added on the $\widetilde{\omega}_C$ field. The *y*-normal velocity streamlines indicate that fresh gas from the central dilution jet are captured by the IRZ, reducing its temperature. The velocity streamlines also indicate that the IRZ consists of two bubbles: a small upstream bubble is located within the injector and its width is found to decrease at its downstream end due to the axial swirler flows, a second large bubble occupies the center of the primary zone. The flow pattern is very similar for all fuels at the exception of the size of the upstream bubble, which is smaller

for Cat-C1. The temperature in the upstream bubble is slightly above the fresh-gas temperature, indicating that the recirculating hot gases are rapidly mixed with fresh gases near the meeting point between the two bubbles. The temperature in the recirculation zones is found to depend on the fuel. Specifically, temperatures in both inner and outer recirculation zones are higher for
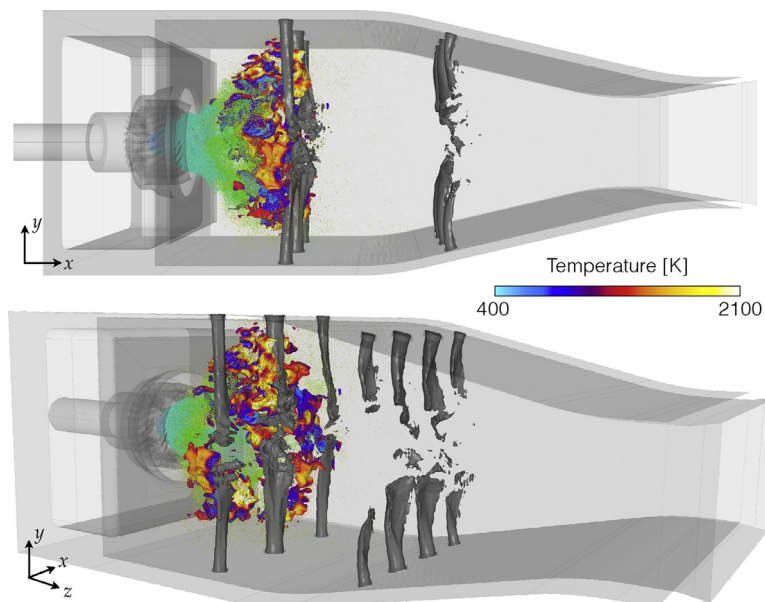

Fig. 9. (color online) Two views showing the combustion chamber for Cat-A2 at $\phi_g = 0.096$. Flame position is materialized by a $\widetilde{\omega}_C = 100$ s^{-1} iso-surface. Grey iso-surfaces at $u_y = \pm 80$ m/s shows the dilution jets.
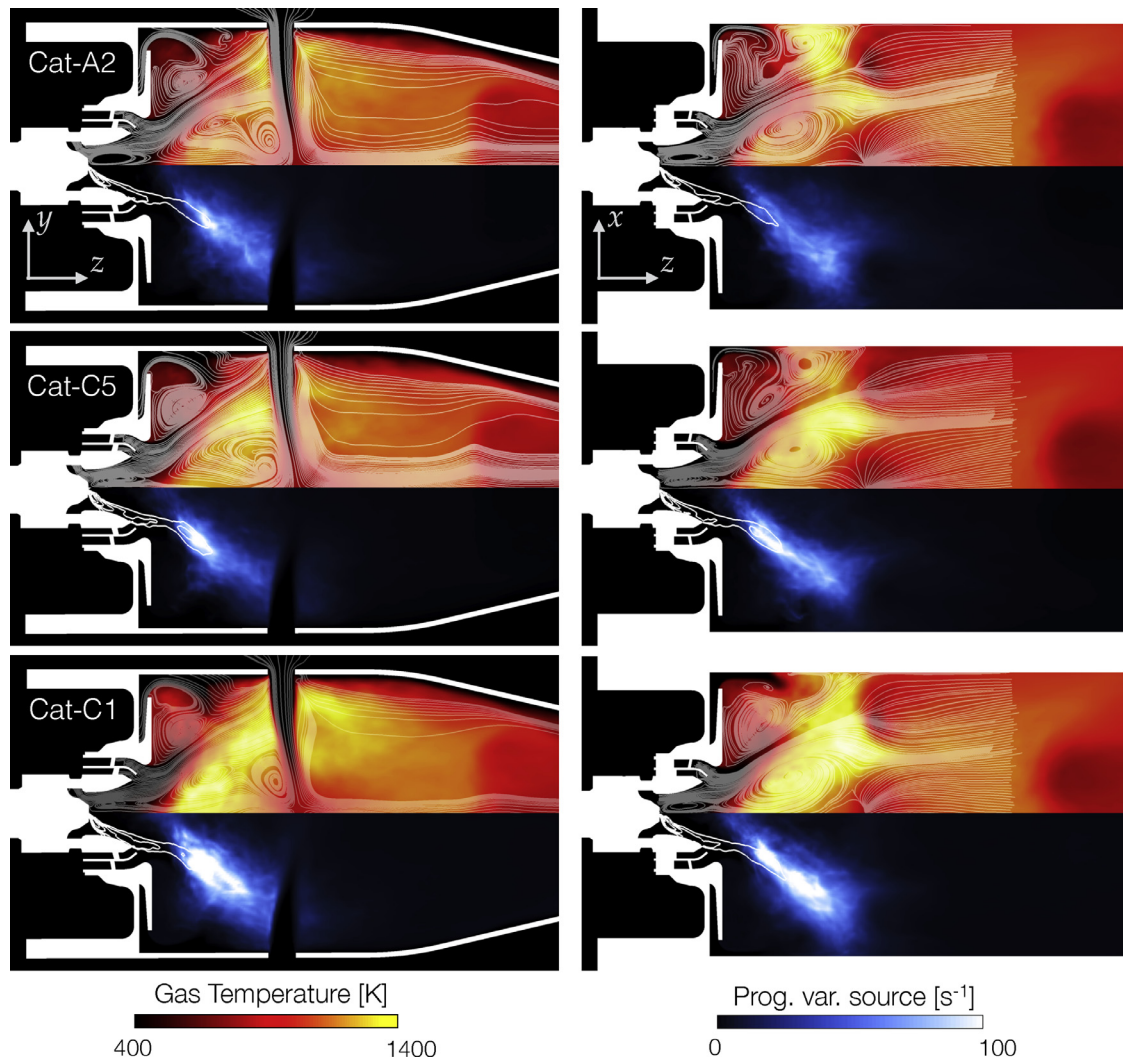
Fig. 10. (color online) Time-averaged temperature (top half) and progress variable source term (bottom half) in a central *x*-normal (left) and *y*-normal (right) cut plane for all fuels. Velocity streamlines are superimposed on the temperature field. Iso-contours of evaporation source term are overlaid on $\tilde{\dot{\omega}}_C$ fields.

Cat-C1 with a larger progress-variable source region in the shear layer between the IRZ and the incoming fresh gas compared to Cat-A2. Note that because of the very lean equivalence ratio, the time-averaged temperature of the IRZ is far below the stoichiometric temperature. Indeed, the equivalence ratio of the primary zone $\phi_{PZ} = 0.381$ (based on the air flowrate from the swirler, the liner cooling and a quarter of the first row of the dilution jet), presented in Table 4, is significantly below stoichiometry. The maximum time-averaged equivalence ratio in the shear layer between the swirled jet and the IRZ does not exceed a value of 0.6. The equilibrium temperature obtained at ϕ_{PZ} is of $\simeq 1337$ K for Cat-A2 and Cat-C5 and $\simeq 1359$ K for Cat-C1.

In previous LES studies of spray flames near LBO [32,33,53], combustion was stabilized by a fuel-rich and hot recirculation zone at the boundary where the flame is located, following the stoichiometric iso-surface. At these conditions, the aerodynamic strain and the small equivalence ratio result in the occurrences of local extinction/re-ignition of the flame surface, identified as precursors of the complete flame blow-out. In the present case, the flow pattern and the low overall equivalence ratio of the primary zone prevent the formation of a rich and hot recirculation bubble. Instead, the flame stabilization is weak and two reaction zones are observed: (i) intermittent diffusion flame fronts are observed, fol-

lowing the stoichiometric mixture fraction iso-surface; (ii) a weak lean premixed flame front is located along the IRZ.

In order to illustrate the formation of diffusion flames, time series of gas temperature and droplet distribution fields in the shear layer between the IRZ and the droplet-laden fresh gas flow are shown in Fig. 11 for Cat-A2 (left) and Cat-C1 (right). The black iso-contour indicates the stoichiometric mixture fraction while the white iso-contour shows the position of the IRZ. Cat-C5 (not shown) has a similar flame stabilization to that of Cat-A2, where flame pockets are formed in the shear layer between the droplet-laden fresh gas flow and the IRZ. Large-scale motion of the shear layer induces entrainment of burnt gases within the incoming flow, promoting evaporation and ignition of droplet packets. These packets are then convected downstream, where they partially recirculate. For Cat-C1, the flame stabilization mechanism is significantly different, as indicated by the presence of stoichiometric mixture fraction all along the zero axial velocity location in Fig. 11. The flame is anchored closer to the nozzle and is less intermittent. This change allows more burnt gases to be recirculated which results in a higher IRZ temperature, enabling faster evaporation and ignition.

To better understand the differences observed on the diffusion flame formation between the three different fuels, the ignition behavior of the coupled liquid/gas is investigated. A 0D pseudo-batch reactor is used to evaluate the effect of the initial droplet size and
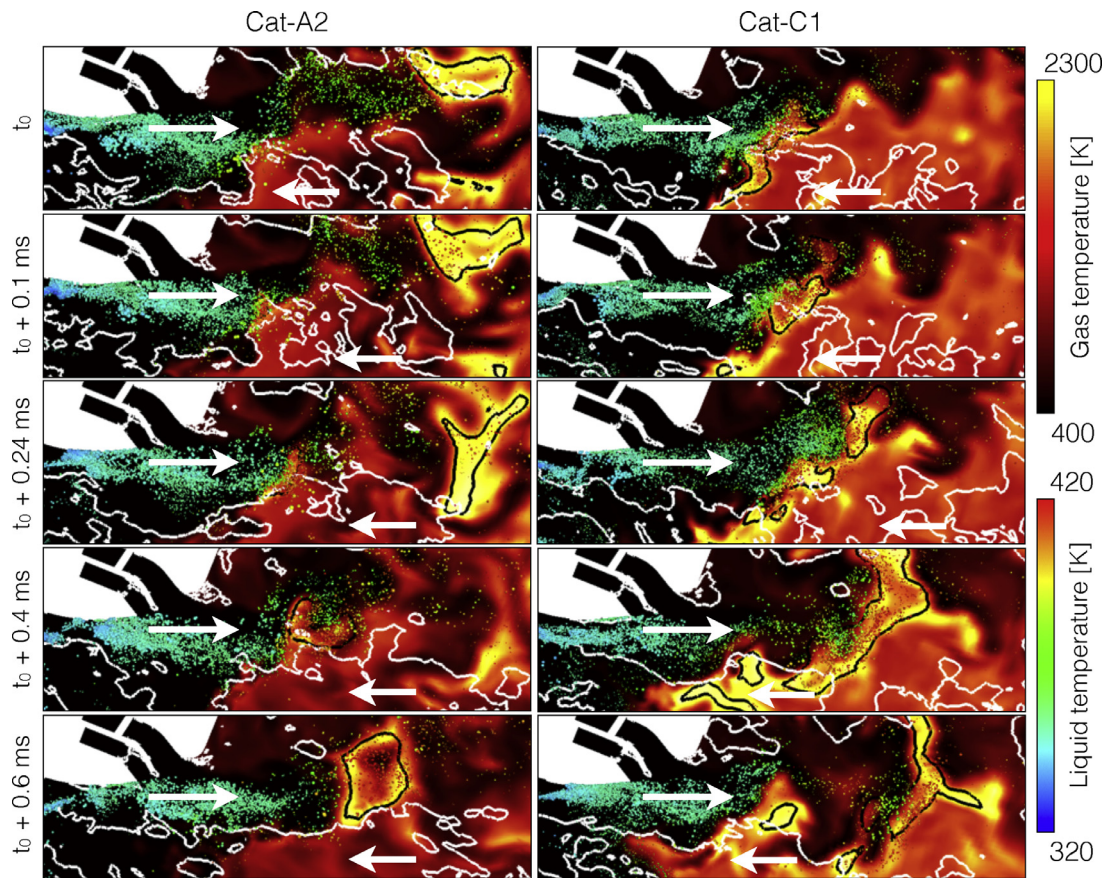
Fig. 11. (color online) Shear layer between the swirled cold air and the IRZ colored by the temperature with overlaid droplets colored by their temperature. Black iso-contours indicate the position of stoichiometric mixture fraction while the white iso-contours correspond to the zero axial velocity.
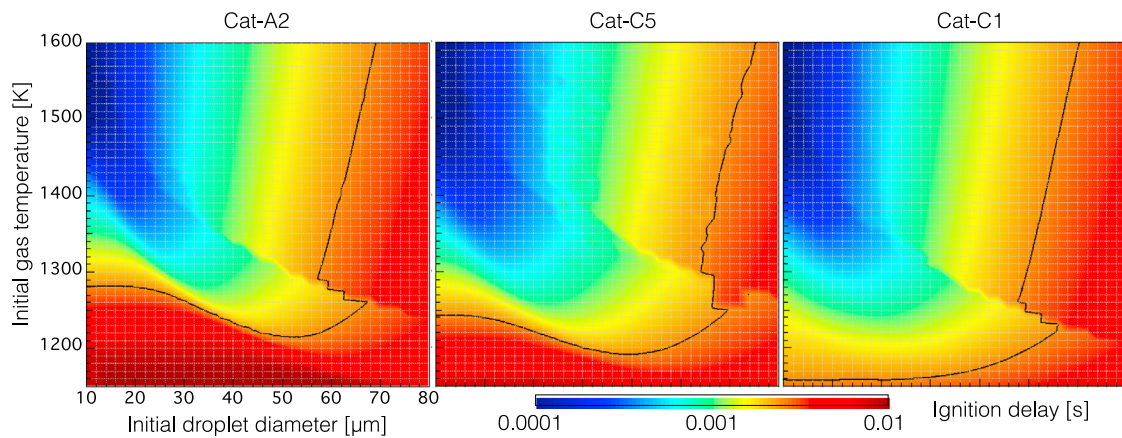

Fig. 12. (color online) Ignition delay maps of two-phase pseudo-batch reactors. The black curve denotes the isoline for $\tau_{sys} = 0.5\tau_{res}$.

initial gas temperature on the ignition delay of the system. This reactor solves the coupled liquid/gas equations [54]. Results are presented in Fig. 12, showing ignition delay maps as a function of initial droplet diameter and initial gas temperature for an overall equivalence ratio of $\phi = 1$. For reference, the black curves represent half the residence time τ_{res}. The ignition delay of the system τ_{sys} is evaluated as the instant at which the maximum heat release rate is reached. The ignition of the system is controlled by two time scales: the ignition delay time τ_{ign} of the pre-vaporized mixture (cf. Fig. 5(b)) and the evaporation time τ_{evap}. Depending on the relative value of the two time scales, two peaks of heat release rate can be observed: fast ignition kinetics can induce a first peak before the complete evaporation of the droplet cloud, followed by a rapid decay of the heat release rate as the fuel is depleted; a second peak can be observed later as the evaporation is enhanced by the increased gas temperature. The sharp transition region observed for all fuels in Fig. 12 corresponds to a change of the maximum heat release rate between the two peaks. A region with high ignition delay ($\tau_{sys} > \tau_{res}/2$) is found for all fuels at low temperature and small droplet diameter, and for large diameters. The minimum of the ignition delay is found in the high temperature/small diameter region for all fuels and extends towards
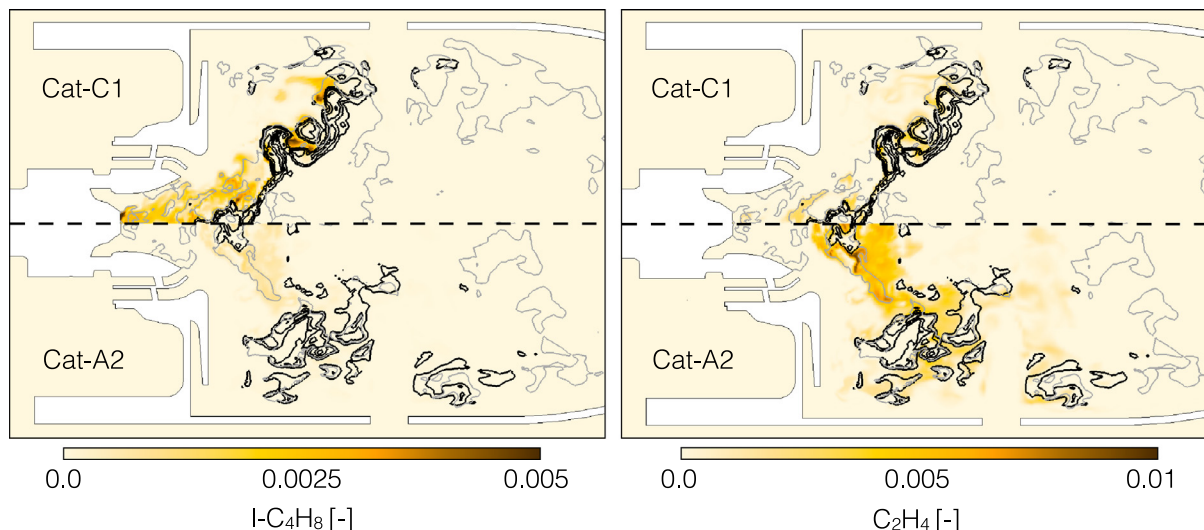
Fig. 13. (color online) Mass fraction of iso-butene (left) and ethylene (right) for Cat-C1 (top row) and Cat-A2 (bottom row). Black lines: iso-contours of $\widetilde{\dot{\omega}}_C$. Grey lines: iso-contours of $\widetilde{Z} = 0.022$.

the large droplet/small temperature region. The large ignition delays observed for small droplet diameters arise from the rapid reduction of the gas temperature induced by evaporation, before the initiation of the ignition. Because of the larger ignition delay time (cf. Fig. 5(b)) for Cat-A2, the region where $\tau_{sys} > \tau_{res}/2$ is larger compared to the two other candidate fuels. At gas temperatures below 1350 K, τ_{sys} exhibits non-monotonic behavior. With increasing droplet diameter, τ_{sys} first decreases since τ_{evap} increases, limiting the temperature decrease prior to the kinetic run-away. This region approximately corresponds to $\tau_{ign} \simeq \tau_{evap}$. As the droplet diameter is further increased, ignition is postponed by the lack of vaporized fuel, resulting in an increase in τ_{sys}. Cat-C1 is found to be the fastest igniting mixture, which is primarily responsible for the change in flame position and structure compared to Cat-A2 and Cat-C5.

The premixed reaction zone results from the partial premixing of air with the evaporated fuel. Small droplets generated by the secondary break-up close to the pressure-swirl nozzle are able to evaporate due to the strong slip velocity. The evaporated fuel interacts with the mildly hot recirculated gas and pyrolysis products are formed upstream of the main flame. Figure 13 shows the mass fraction fields of two pyrolysis products (namely ethylene (C_2H_4) and iso-butene (i-C_4H_8)) near the injection system for Cat-A2 and Cat-C1. Black iso-contours show the position of the reaction zone ($\widetilde{\dot{\omega}}_C$ ranging from 20 s^{-1} to 1000 s^{-1}) while grey lines are the $\widetilde{Z} = 0.022$ iso-contours, used as an indicator for the lean flammability limit (LFL). For Cat-A2, mixtures below the flammability limit are more frequently observed in the IRZ and the premixed flame front is quenched. Furthermore, reactive fronts are found around $\widetilde{Z} = 0.022$ in the case of Cat-C1, whereas the reaction is extinguished for Cat-A2. This difference can be related to the change in pyrolysis yield between the candidate fuels (Cat-C5 as a similar yield as Cat-A2). Figure 13 shows that the mass fraction of C_2H_4 is much higher for Cat-A2 compared to Cat-C1 while the opposite trend is observed for i-C_4H_8. This difference in composition induces a shift of the LFL between the two fuels since ethylene has a higher LFL than iso-butene [55]. Note that the reaction rate in the lean premixed flame fronts is much smaller than the one observed in the diffusion flame described above and that the flame is sustained by the hot gases generated by the diffusion flame and recirculated by the IRZ.

Investigation of the stable case close to the LBO-limit indicates that for all three selected candidate fuels, most of the reaction oc-

curs in the primary zone at the interface between the IRZ and the incoming spray/air mixture. The analysis of the flame reveals two reaction zones: an intermittent diffusion flame forming around droplet clouds, and a weak lean premixed flame front. In accordance with experiments, only marginal fuel effects on the flame position are observed for Cat-C1, where the flame is found to sit closer to the injection system and to have higher OH*-emissions levels. These differences are related to the faster ignition of the spray/air mixture and the extension of the flammability limits induced by the change in pyrolysis yield.

6. Lean blow-out characteristics

In the present experimental campaign, LBO is triggered by progressively reducing the fuel flow rate by 1.6 mg/s^2 until LBO occurs (over a maximum duration of 240 s). This method contrasts with experiments performed in academic configurations for which numerical simulations were performed [32,33] where blow-off is triggered by an increase in the air flow rate. Owing to the computational cost of the simulations, reproducing the experimental approach is currently not affordable with LES. Instead, in the present study LBO is induced by a step decrease of the fuel injection rate, starting from the stable operating condition presented in Section 5. In order to evaluate the LBO-limit, the final value of the equivalence ratio at each step is obtained by a bisection method. This approach allows to bound the LBO-limit and to adjust the precision of this estimate to the available computational resources. After this step decrease in the fuel mass flow rate, simulations are continued over at most four residence times (20 ms) to observe blow out. Note that it is possible for blow-off to occur beyond this 20 ms window; however, for the cases observed to be stable, all combustion indicators presented in Fig. 14 are found to be statistically stationary. Since each equivalence ratio step is only performed once, the stochasticity of the LBO is not addressed in the simulations.

A summary of simulations performed for all candidate fuels is presented in Table 5. Experiments indicate that, in comparison with Cat-A2, the LBO-limit for Cat-C1 ($\phi_{LBO,exp} = 0.0869$) is 7.8% higher and Cat-C5 ($\phi_{LBO,exp} = 0.0825$) is 2.4% higher. In contrast, LES-results indicate that the LBO-limit of Cat-A2 and Cat-C5 is between $\phi_g = 0.09$ and $\phi_g = 0.093$ while that of Cat-C1 is between $\phi_g = 0.085$ and $\phi_g = 0.09$. This discrepancy could potentially be the consequence of the different approaches used in experiments and simulations to determine the LBO-limit. Note also that experi-
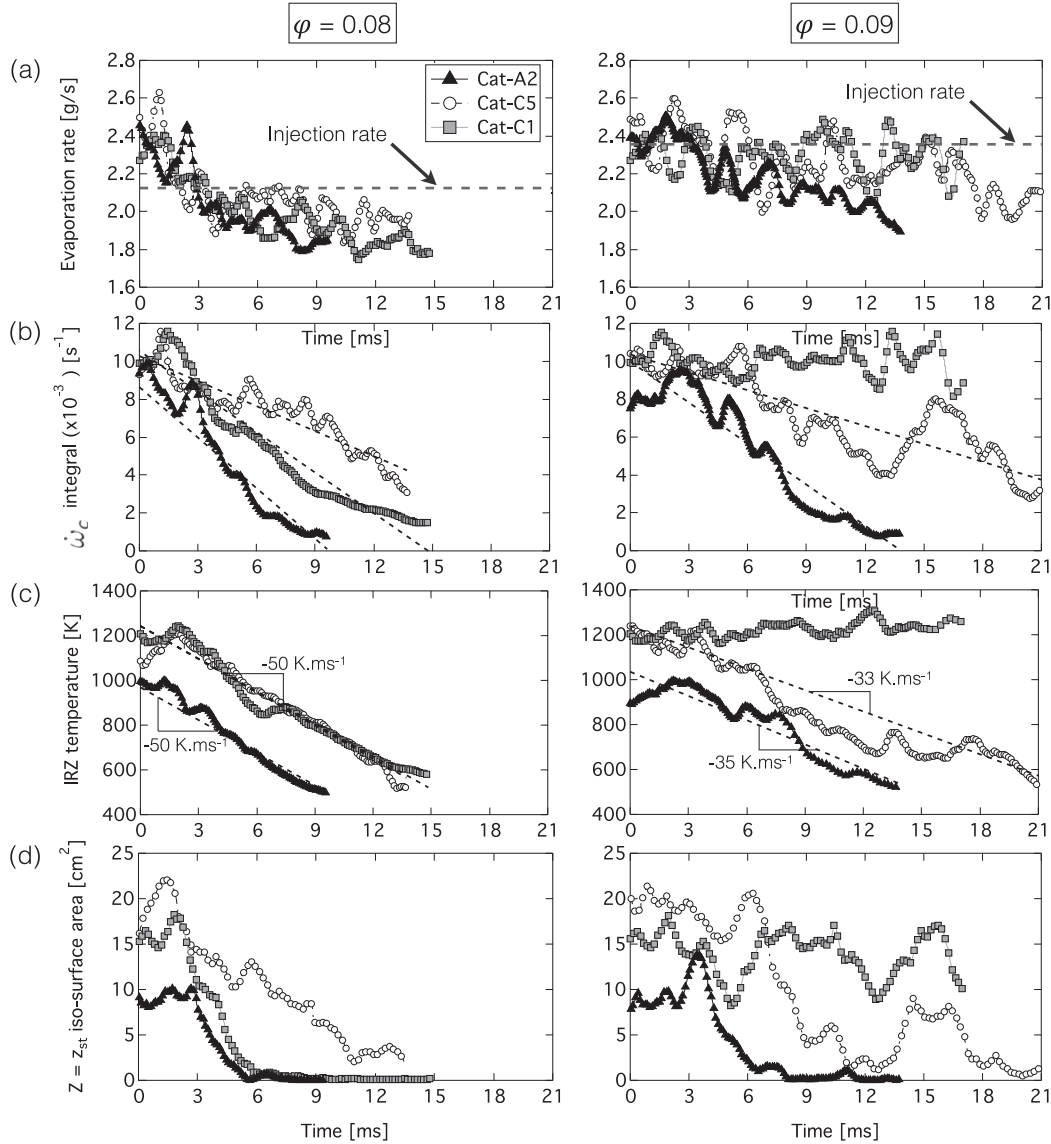
Fig. 14. Temporal evolution of: (a) evaporation rate and (b) integral of progress variable source term in the primary zone, (c) mean IRZ temperature and (d) area of the $\widetilde{Z} = Z_{st}$ iso-surface for final equivalence ratios of 0.08 (left) and 0.09 (right).

Table 5

Summary of operating conditions studied in LES along with experimental observations: ticks indicate stable operating point, crosses indicate blow-off conditions.

ϕ_g	Cat-A2		Cat-C5		Cat-C1	
	Exp.	LES	Exp.	LES	Exp.	LES
0.096	✓	✓	✓	✓	✓	✓
0.093	✓	✓	✓	✓	✓	–
0.090	✓	✗	✓	✗	✓	✓
0.085	✓	–	✓	–	✗	✗
0.080	✗	✗	✗	✗	✗	✗

ments show small differences between the LBO-limit of the candidate fuels, and comparable differences are observed from the simulations. The effect of the fuel on the LBO-limit observed in both experiments and simulations is much smaller than the one obtained in Section 4.2 from empirical correlations. A fundamental limitation of these correlations stems from the fact that the fuel effect on each process is taken into account independently, without

considering non-linear interactions between physical and chemical processes as illustrated in the coupled system presented in Fig. 12.

At $t_0 = 0$ ms, the liquid injection rate is reduced from its initial value corresponding to a global equivalence ratio of 0.096 to the target value closer or beyond the blow-off limit. The subsequent transient behavior is investigated by the analysis of the temporal evolution of several key indicators of the flame and combustor state. The integral of the progress variable source term in the primary zone, $\int_{V_{PZ}} \widetilde{\dot{\omega}}_C \, dV$, is used to evaluate the combustor stability while the integrated evaporation rate (in the primary zone) is an indicator for the availability of vaporized fuel. The integral over the primary zone is preferred to that over the entire combustor as the flame stability is controlled by the recirculation of burnt gases. As illustrated in Section 5.2, flame stabilization is closely related to the formation of diffusion flames around rich regions of droplets. The temporal evolution of the stoichiometric iso-surface area ($\widetilde{Z} = Z_{st}$) is computed to characterize the occurrence of diffusion flames. Finally, the mean temperature of the IRZ, defined as the negative axial velocity region nested in the primary zone, is recorded to characterize the combustor state. In-
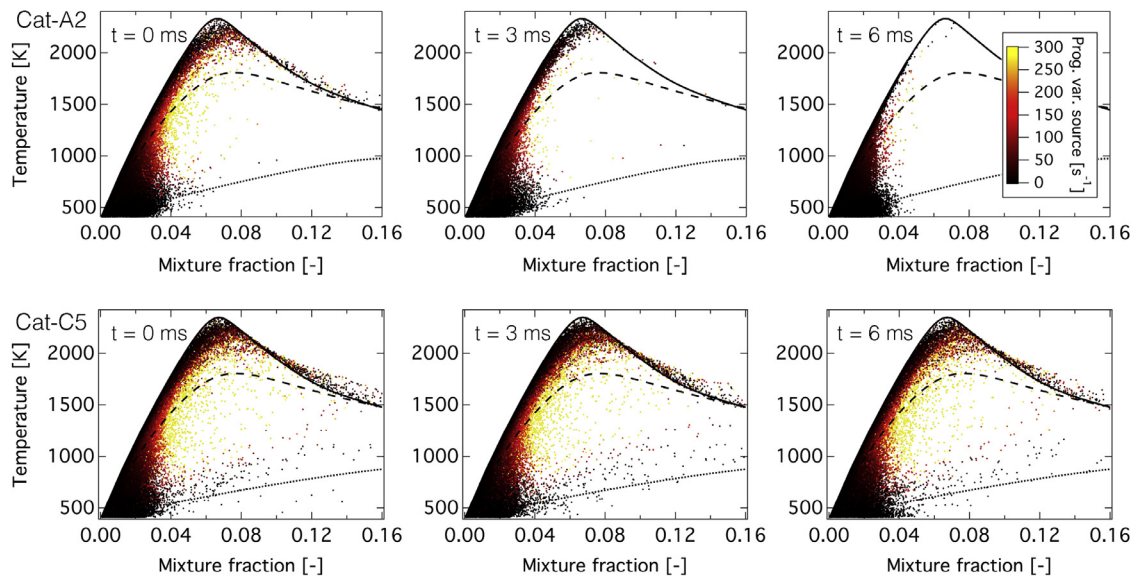
Fig. 15. (color online) Scatterplots of temperature versus mixture fraction for Cat-A2 (top) and Cat-C5 (bottom) at (left) $t = 0$ ms, (middle) $t = 3$ ms, and (right) $t = 6$ ms.

deed, experimental studies in swirled combustors [24,26] indicate that both the IRZ temperature as well as the position and oscillations of the flame root are causal to the occurrence of blow-out in gaseous burners. The temporal evolutions of these four indicators in the cases with final equivalence ratio of 0.08 and 0.09 are presented in Fig. 14 for all three candidate fuels. The dashed lines in Fig. 14(b) and (c) correspond to linear fits through the data.

Two videos, showing the transient behavior of the combustor during blow-off, are provided as supplementary material. They show the temperature field in a central x-normal cut plane along with the spray colored by the liquid temperature from 3.9 ms before the LBO-triggering time until the mean temperature in the IRZ decreases below 600 K. The first video [LBO_CatA2_vs_CatC5.mp4] compares the blow-off event for Cat-A2 and Cat-C5 candidate fuels at $\phi_g = 0.08$ while the second video [LBO_CatC1_0p08_vs_0p09.mp4] shows a comparison of the transient behavior of Cat-C1 for equivalence ratios of $\phi_g = 0.08$ and $\phi_g = 0.09$ starting from the same initial conditions.

The comparison of the behavior of the Cat-A2 and Cat-C5 fuel candidates shows that the spray dynamics is not affected by the change in injection rate. After $t = t_0$, the temperature of the recirculation zone decreases for Cat-A2 while for Cat-C5 large burnt gas pockets are recirculated, maintaining a higher temperature in the IRZ. The comparison of the two fuel candidates shows that this is a direct consequence of the difference in the flame position, located upstream for Cat-C5. The second video shows, in mirrored views, simulations for cases with constant equivalence ratio of $\phi_g = 0.08$ (top) and $\phi_g = 0.09$ (bottom). Until 2 ms after the change in liquid injection rate, the top and bottom fields are similar. As time proceeds, differences arise in the flame evolution between both cases; eventually the case with $\phi_g = 0.09$ shows formation of flames around the incoming droplets where the case with $\phi_g = 0.08$ shows none. This is a direct consequence of the larger droplet density for the case with $\phi_g = 0.09$ which allows locally to reach near stoichiometric conditions. This leads to a stable flame, while the case with $\phi_g = 0.08$ blows off completely.

For the condition with $\phi_g = 0.08$, within 15 ms all the indicators exhibit a rapid decay, indicating blow-off. Blow-off is consid-

ered complete when the mean IRZ temperature drops below 600 K. At stable conditions, the evaporation rate is found to oscillate at the frequency of the PVC and the oscillations remain during the transient simulation (cf. in Fig. 14(a)). Note that not all the liquid fuel is evaporated in the primary zone due to the presence of large droplets. Approximately 2–3 ms after t_0, the evaporation rate has decreased below the injection rate for all fuels and continues to decrease as time proceeds. Evaporation does not fully cease even after blow-off due to the preheating of the fresh gas and the accumulation of droplets in the IRZ. The reduction of the evaporation rate leads to a reduction in the overall reaction rate with very little delay compared to the evaporation since evaporation occurs close to the reaction zone. The linear fits indicate that Cat-A2 exhibits the fastest rate of decay while Cat-C5 is the slowest. The effect of the lower evaporation rate on the flame structure is illustrated in Fig. 15, comparing scatter plots of temperature versus mixture fraction at three instances during the blow-off sequence for Cat-A2 and Cat-C5. The full, dashed and dotted lines represent laminar counterflow diffusion flames at equilibrium, close to extinction and on the mixing branch, respectively. Initially, the mixture fraction is below $Z = 0.16$ and the gas mixture corresponds to the adiabatic composition for both fuels. Due to the overall lean conditions, the mixture fraction gradients are small and the effect of scalar dissipation rate is limited. As time proceeds, the mixture fraction range reduces for Cat-A2 until the evaporation rate is insufficient to have locally stoichiometric pockets. This is illustrated for all candidate fuels in Fig. 14(d) where the size of the stoichiometric mixture fraction iso-surfaces are found to rapidly decrease for the Cat-A2 and Cat-C1 candidate fuels. In contrast, the faster evaporation rate of Cat-C5 induces the presence of stoichiometric mixture fraction for longer time. The mean temperature in the IRZ shows a similar decay rate for all three candidate fuels but it takes approximately 6 ms ($\simeq \tau_{res}$) longer for the mean temperature to drop below 600 K for Cat-C5 and Cat-C1 than Cat-A2. This delay can be attributed to two effects: (i) the IRZ temperature is found to stay close to its stable operating point during 4 ms for Cat-C5 and Cat-C1 but only during 2 ms for Cat-A2; (ii) the initial IRZ temperature is higher for Cat-C5 and Cat-C1. Since the IRZ temperature oscillates, this delay would change if LBO is triggered at another time. At $\phi_g = 0.09$, Cat-A2 and Cat-C5 candidate fuels exhibit blow-off while Cat-C1 remains stable. The final injection rate

is within the range of evaporation rate fluctuations at stable conditions so that a clear reduction in evaporation rate is not observed. The duration of the time delay between the change in liquid injection rate and a significant decrease of the indicators is observed. The rate of decay of the overall reaction rate is found to be lower than for the condition with $\phi_g = 0.08$ for both unstable candidate fuels and Cat-A2 also extinguish faster than Cat-C5. The temporal evolution also shows large fluctuations, especially for Cat-C5, associated with partial recovery of the flame front. Similarly to the case with $\phi_g = 0.08$, the decay rate of the mean temperature in the IRZ is found to be very similar for Cat-A2 and Cat-C5.

From the analysis of the blow-off transients, it can be concluded that Cat-A2 exhibits the fastest blow-off even though Cat-A2 and Cat-C5 are found to have a very similar LBO-limit. Cat-C1 is found to be faster to blow off than Cat-C5 at $\phi_g = 0.08$ but its LBO-limit is lower than Cat-C5. This suggests that the blow-off decay rate cannot be used as an indicator for the blow-off limit.

7. Conclusions

In this paper, the capability of LES in describing the sensitivity of physico-chemical properties of representative aviation fuels on stable combustion conditions near blow-out and transient conditions during lean blow-out (LBO) is investigated. Simulations are performed in a referee combustor rig that was experimentally investigated at the Air Force Research Laboratory. This rig was designed to reproduce relevant features of realistic aeronautical combustors in terms of liquid-fuel injection system, RQL-design, and air flow staging. This study focused on a comparative analysis between a conventional Jet-A fuel (Cat-A2) and two alternative fuel candidates having a fast evaporation behavior (Cat-C5) and a lower derived cetane number (Cat-C1). Prior to performing LES-calculations, investigations were conducted to characterize effects of the physico-chemical properties on spray formation, droplet evaporation, combustion characteristics and LBO-behavior. These investigations showed that the Cat-C5 candidate fuel differs from Cat-A2 mainly by its physical properties while the difference for Cat-C1 arises from its chemical properties. Using widely employed empirical correlations, strong fuel effects were predicted on the LBO-limit.

This initial investigation was followed by performing a series of LES-calculations for each fuel to examine the combustion characteristics at stable conditions near lean blow-out in order to establish an understanding of the stabilization mechanisms. Simulation results were compared against experimental data from PDPA-measurements and chemiluminescence emissions. LES-results were shown to be in good agreement with available experimental data in terms of spray angle, droplet velocity, and flame position. Analysis of the flame at this near-blow-out condition indicated the presence of two distinct reaction regions, namely (i) the formation of intermittent diffusion flames around dense droplet clouds promoting the formation of fuel-rich pockets and (ii) a very lean premixed flame burning partially pyrolized fuel. The premixed flame was sustained by the recirculation of hot gases from the diffusion flame. The diffusion flame controls the fuel-evaporation and the partial pyrolysis of the fuel. The simulations showed that the Cat-C1 candidate fuel exhibits faster ignition and a widening of the flammability limit, due to changes in the pyrolysis products. The faster evaporation of Cat-C5 was found to have only marginal effects on the flame characteristics.

Finally, a series of transient LES-calculations were performed for all candidate fuels to provide a better understanding of the blow-out mechanism. In these simulations, blow-out was modeled by an instantaneous reduction in the fuel injection rate, starting from a stable operating condition. These transient blow-out simulations showed that the reduction of the recirculation temperature slows the evaporation process, reducing the availability of the gaseous fuel, eventually leading to blow-off. The LBO-limits for all candidate fuels were found to be very close, with Cat-C1 being slightly more stable. In contrast with the results from empirical correlations, only marginal fuel effects on the LBO-limit were observed for both experiments and LES, showing the limitations of such correlations in evaluating fuel effects at the design stage. The analysis of the transient LES-data showed that Cat-A2 is blowing off faster than the other two fuels. The faster evaporation of the Cat-C5 candidate fuel allows to maintain a sufficient evaporation rate longer while the change in flame position induced by Cat-C1 kinetics allows for a stronger flame piloting.

While good agreement between measured and predicted LBO-trends for Cat-A2 and Cat-C5 were obtained, the LES-prediction of the LBO-limit for Cat-C1 differed from the experiments, indicating that further studies are needed to evaluate the sensitivity with respect to the submodels employed in this study. The spray is hereby expected to be the main source of uncertainty. Specifically, the LBO-limit of all candidate fuels is expected to be sensitive to the Sauter mean diameter, and a more detailed consideration of the multicomponent fuel properties on the evaporation and the combustion could contribute to further changes in the relative differences between the LBO-limits of the candidate fuels [54]. The strong dependency to the spray also suggests that a higher fidelity spray/flame combustion model [41] could further improve the LES accuracy.

Appendix A. Specification of liquid-fuel properties

The liquid properties are fitted through experimental data obtained at atmospheric conditions. Physical properties are then extrapolated from the experimental data range in the LES solver. Figure 16 shows the evolution of liquid density ρ_l, liquid heat capacity c_l, surface tension σ_l, liquid dynamic viscosity μ_l, saturation vapor pressure P_{vs}, and latent heat of vaporization (LHV) Δ_{Hv} as a function of temperature for the three selected fuel candidates.

The functional form and the values of the coefficients obtained for each fuel are summarized in Table 6. The functional form of the LHV is obtained from Yaws' Handbook of thermodynamic and physical properties [56] and the value at 298 K obtained from the fuel composition. The critical temperature of the candidate fuels is estimated using the boiling point defined as the 100% vapor fraction recovery temperature and following the method detailed in Watson [57] (also used in the CRC Handbook for aviation).
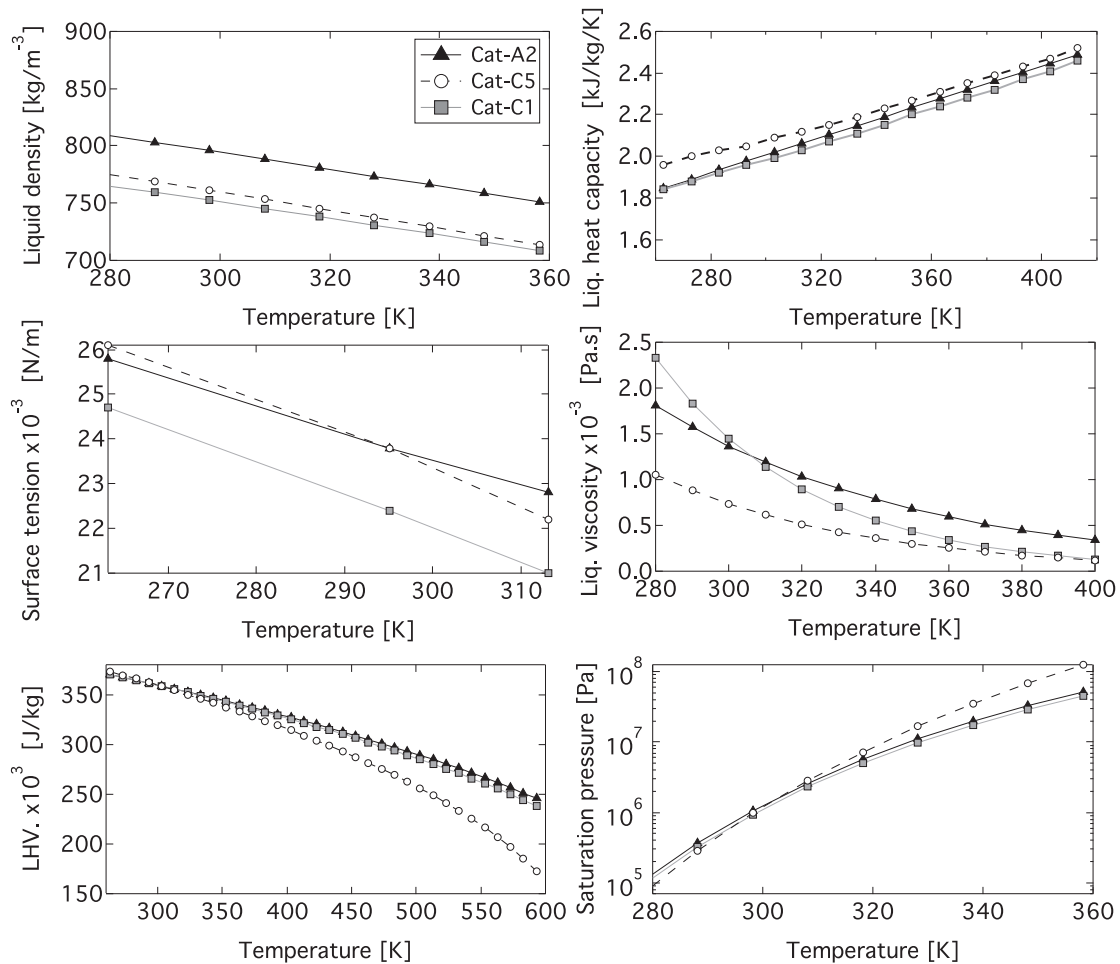
Fig. 16. Candidate fuels physical properties as function of temperature obtained from experiments (except the latent heat of evaporation).

Table 6
Functional form and coefficients for the liquid physical properties obtained by fitting experimental data (except LHV). Temperature in the functional form is in units of K.

	Units	Cat-A2	Cat-C5	Cat-C1
Density: ρ_L	[kg/m³]		$a_\rho T + b_\rho$	
a_ρ		−0.74617	−0.78550	−0.72
b_ρ		1018.26	995.11	967.01
Heat Capacity: c_L	[kJ/kg/K]		$a_{c_L} T + b_{c_L}$	
a_{c_L}		0.00428	0.00370	0.00410
b_{c_L}		0.723	0.973	0.753
Surface tension: σ	[N/m]		$a_\sigma T + b_\sigma$	
a_σ		6.03e-5	7.73e-5	7.38e-5
b_σ		0.04165	0.04648	0.04412
Viscosity: μ_L	[Pa.s]		$b_\mu e^{a_\mu T}$	
a_μ		−0.01394	−0.01795	−0.02393
b_μ		0.08949	0.016018	1.89212
Vapor pressure: P_{vs}	[Pa]		$10^{\wedge}(a_1 + a_2/T + a_3 \log(T) + a_4 T)$	
a_1		28.95	27.6	28.9
a_2		−3000.4	−3000.0	−3000.4
a_3		−6.5	−6.4	−6.5
a_4		−4.00e-4	3.00e-3	−4.00e-4
LHV: Δ_{Hv}	[J/kg]		$\Delta_{Hv,298}[(T_c - T)/(T_c - 298)]^{0.375}$	
$\Delta_{Hv,298}$		3.80e5	3.76e5	3.60e5
T_c		760.4	641.2	740.2

Appendix B. Supplementary material

Supplementary data associated with this article consists of the following:

- Composition of the three candidate fuels (Candidate composition.xlsx).
- A video (LBO CatA2 vs CatC5.mp4) showing the comparative time evolution of the gas temperature in a central cut-plane for both Cat-A2 and Cat-C5 during a blow-off event.
- A video (LBO CatC1 0p08 vs 0p09.mp4) comparing the response of Cat-C1 flame to a reduction in global equivalence ratio from 0.96 to 0.9 and 0.8, showing time evolution of the gas temperature in a central cut-plane.

Supplementary data can be found in the online version.

Supplementary material

Supplementary material associated with this article can be found, in the online version, at 10.1016/j.combustflame.2017.02.035.

References

[1] L.Q. Maurice, H. Lander, T. Edwards, W. Harrison, Advanced aviation fuels: a look ahead via a historical perspective, Fuel 80 (5) (2001) 747–756.
[2] T. Edwards, Advancements in gas turbine fuels from 1943 to 2005, J. Eng. Gas Turbines Power 129 (1) (2007) 13–20.

[3] S. Blakey, L. Rye, C.W. Wilson, Aviation gas turbine alternative fuels: a review, Proc. Combust. Inst. 33 (2) (2011) 2863–2885.

[4] M. Colket, T. Edwards, S. Williams, N.P. Cernansky, D.L. Miller, F. Egolfopoulos, P. Lindstedt, K. Seshadri, F.L. Dryer, C.K. Law, D. Friend, D. B. Lenhert, H. Pitsch, A. Sarofim, M. Smooke, W. Tsang, Development of an experimental database and kinetic models for surrogate jet fuels, 45th AIAA Aerospace Sciences Meeting and Exhibit, AIAA paper no. 2007-0770 (2007).

[5] M. Colket, J. Heyne, M. Rumizen, M. Gupta, A. Jardines, T. Edwards, W.M. Roquemore, G. Andac, R. Boehm, J. Zelina, J. Lovett, J. Condevaux, S. Bornstein, N. Rizk, D. Turner, C. Graves, M.S. Anand, R. Williams, F. Xu, J. Tishkoff, C. Li, J. Moder, R. Anthenien, D. Friend, P. Chu, R. Kamin, Z. Haq, P. Serino, M. Domen, C.-B. M. Kweon, V. Sankaran, J. Cohen, W. Chishty, P. Canteenwalla, A. Corber, An overview of the national jet fuels combustion program, 54th AIAA Aerospace Sciences Meeting and Exhibit, AIAA paper no. 2016–0177 (2016).

[6] M. Braun-Unkhoff, T. Kathrotia, B. Rauch, U. Riedel, About the interaction between composition and performance of alternative jet fuels, CEAS Aeronaut. J. 7 (1) (2015) 83–94.

[7] D.L. Daggett, R.C. Hendricks, R. Walther, E. Corporan, Alternate fuels for use in commercial aircraft, 8, The Boeing Company, 2007.

[8] ASTM, Standard practice for qualification and approval of new aviation turbine fuels and fuel additives, Technical Report ASTM D4054, ASTM, 2014.

[9] J.M. Beér, N.A. Chigier, Combustion aerodynamics, Krieger, 1972.

[10] S. Plee, A. Mellor, Characteristic time correlation for lean blowoff of bluff–body-stabilized flames, Combust. Flame 35 (1979) 61–80.

[11] D.R. Ballal, A.H. Lefebvre, Ignition and flame quenching of flowing heterogeneous fuel-air mixtures, Combust. Flame 35 (1979) 155–168.

[12] J.P. Longwell, Flame stabilization by bluff bodies and turbulent flames in ducts, Symp. (Int.) Combust. 4 (1) (1953) 90–97.

[13] E. Zukoski, Flame stabilization on bluff bodies at low and intermediate Reynolds numbers, California Institute of Technology, 1954 (Phd thesis).

[14] S. Yagamuchi, N. Ohiwa, T. Hasegawa, Structure and blow-off mechanism of rod-stabilized premixed flame, Combust. Flame 62 (1) (1985) 31–41.

[15] S. Shanbhogue, S. Husain, T. Lieuwen, Lean blowoff of bluff body stabilized flames: Scaling and dynamics, Prog. Energy Combust. Sci. 35 (2009) 98–120.

[16] A.H. Lefebvre, Fuel effects on gas turbine combustion – ignition, stability, and combustion efficiency, J. Eng. Gas Turbines Power 105 (1985) 24–37.

[17] D. Feikema, R.-H. Chen, J.F. Driscoll, Enhancement of flame blowout limits by the use of swirl, Combust. Flame 80 (2) (1990) 183–195.

[18] A. Ateshkadi, V. McDonell, G.S. Samuelsen, Lean blowout model for a spray–fired swirl-stabilized combustor, Proc. Combust. Inst. 28 (2000) 1281–1288.

[19] S. Marinov, M. Kern, N. Zarzalis, P. Habisreuther, A. Peschiulli, F. Turrini, O.N. Sara, Similarity issues of kerosene and methane confined flames stabilized by swirl in regard to the weak extinction limit, Flow Turbul. Combust. 89 (2012) 73–95.

[20] D. Cavaliere, J. Kariuki, E. Mastorakos, A comparison of the blow-off behaviour of swirl-stabilized premixed, non-premixed and spray flames, Flow Turbul. Combust. 91 (2013) 347–372.

[21] C. Moses, D. Naegeli, Fuel property effects on combustor performance, ASME 1979 International Gas Turbine Conference and Exhibit and Solar Energy Conference, Paper No. 79-GT-178 (1979).

[22] J. Blust, D. Ballal, G. Sturgess, Fuel effects on lean blowout and emissions from a well-stirred reactor, J. Propuls. Power 15 (2) (1999) 216–223.

[23] T. Lieuwen, V. McDonell, E. Petersen, D. Santavicca, Fuel flexibility influences on premixed combustor blowout, flashback, autoignition, and stability, J. Eng. Gas Turbines Power 130 (1) (2008) 011506.

[24] T. Muruganandam, J. Seitzman, Origin of lean blowout precursors in swirled gas turbine combustors, 43th AIAA Aerospace Sciences Meeting and Exhibit, AIAA-paper 2005-1163 (2005).

[25] T. Muruganandam, J. Seitzman, Fluid mechanics of lean blowout precursors in gas turbine combustors, Int. J. Spray Combust. Dyn. 4 (1) (2012) 29–60.

[26] M. Stöhr, I. Boxx, C. Carter, W. Meier, Dynamics of lean blowout of a swirl-stabilized flame in a gas turbine model combustor, Proc. Combust. Inst. 33 (2011) 2953–2960.

[27] J. Kariuki, J.R. Dawson, E. Mastorakos, Measurements in turbulent premixed bluff body flames close to blow-off, Combust. Flame 159 (8) (2012) 2589–2607.

[28] J. Kariuki, A. Dowlut, R. Balachandran, E. Mastorakos, Heat release imaging in turbulent premixed ethylene–air flames near blow-off, Flow Turbul. Combust. 96 (4) (2016) 1039–1051.

[29] J. Dawson, R. Gordon, J. Kariuki, E. Mastorakos, A. Masri, M. Juddoo, Visualization of blow-off events in bluff-body stabilized turbulent premixed flames, Proc. Combust. Inst. 33 (1) (2011) 1559–1566.

[30] M. Boileau, G. Staffelbach, B. Cuenot, T. Poinsot, C. Bérat., LES of an ignition sequence in a gas turbine engine, Combust. Flame 154 (1) (2008) 2–22.

[31] P. Wolf, G. Staffelbach, L.Y.M. Gicquel, J.-D. Müller, T. Poinsot, Acoustic and large eddy simulation studies of azimuthal modes in annular combustion chambers, Combust. Flame 159 (11) (2012) 3398–3413.

[32] A. Tyliszczak, D. Cavaliere, E. Mastorakos, LES/CMC of blow-off in a liquid fueled swirl burner, Flow Turbul. Combust. 92 (2014) 237–267.

[33] H. Zhang, E. Mastorakos, Prediction of global extinction conditions and dynamics in swirling non-premixed flames using LES/CMC modelling, Flow Turbul. Combust. 96 (4) (2016) 863–889.

[34] F. Ham, K. Mattsson, G. Iaccarino, P. Moin, Towards time-stable and accurate LES on unstructured grids, Complex Effects in Large Eddy Simulations, Springer (2007), pp. 235–249.

[35] Y.C. See, M. Ihme, Large eddy simulation of a partially-premixed gas turbine model combustor, Proc. Combust. Inst. 35 (2) (2015) 1225–1234.

[36] F. Nicoud, F. Ducros, Subgrid-scale stress modelling based on the square of the velocity gradient tensor, Flow Turbul. Combust. 62 (3) (1999) 183–200.

[37] C.D. Pierce, P. Moin, Progress-variable approach for large-eddy simulation of non-premixed turbulent combustion, J. Fluid Mech. 504 (2004) 73–97.

[38] M. Ihme, C.M. Cha, H. Pitsch, Prediction of local extinction and re-ignition effects in non-premixed turbulent combustion using a flamelet/progress variable approach, Proc. Combust. Inst. 30 (2005) 793–800.

[39] M. Ihme, L. Shunn, J. Zhang, Regularization of reaction progress variable for application to flamelet-based combustion models, J. Comput. Phys. 231 (2012) 7715–7721.

[40] P. Moin, S.V. Apte, Large-eddy simulation of realistic gas turbine combustors, AIAA J. 44 (4) (2006) 698–708.

[41] B. Franzelli, A. Vie, M. Ihme, On the generalisation of the mixture fraction to a monotonic mixing-describing variable for the flamelet formulation of spray flames, Combust. Theory Model. 19 (2015) 773–806.

[42] R.S. Miller, K.G. Harstad, J. Bellan, Direct numerical simulations of supercritical fluid mixing layers applied to heptane-nitrogen, J. Fluid Mech. 436 (2001) 1–39.

[43] S.V. Apte, M. Gorokhovski, P. Moin, LES of atomizing spray with stochastic modeling of secondary breakup, Int. J. Multiph. Flow 29 (9) (2003) 1503–1522.

[44] D. Kim, F. Ham, H. Le, M. Herrman, X. Li, C. Soteriou, W. Kim, High-fidelity simulation of atomization in a gas turbine injector high shear nozzle, ILASS Proceedings Americas 26th Liquid Atomization and Spray Systems (2014).

[45] A.H. Lefebvre, Atomization and sprays, Hemisphere, 1989.

[46] H. Wang, R. Xu, R.K. Hanson, D.F. Davidson, C.T. Bowman, A HyChem model of jet fuel combustion, 2015 (unpublished).

[47] H. Wang, E. Dames, B. Sirjean, D.A. Sheen, R. Tangko, A. Violi, J.Y.W. Lai, F.N. Egolfopoulos, D.F. Davidson, R.K. Hanson, C.T. Bowman, C.K. Law, W. Tsang, N.P. Cernansky, D.L. Miller, R.P. Lindstedt, A high-temperature chemical kinetic model of n-alkane (up to n-dodecane), cyclohexane, and methyl-, ethyl-, n-propyl and n-butyl-cyclohexane oxidation at high temperatures, JetSurF version 2.0 (2010) (http://web.stanford.edu/group/haiwanglab/JetSurF/JetSurF2.0/index.html).

[48] T. Buschhagen, R.Z. Zhang, A.J. Bokhart, R. Gejji, S.V. Naik, R.P. Lucht, J.P. Gore, P.E. Sojka, C.D. Slabaugh, S. Meyer, Effect of aviation fuel type and fuel injection conditions on non-reacting spray characteristics of a hybrid airblast fuel injector, 54th AIAA Aerospace Sciences Meeting and Exhibit, AIAA-paper no. 2016-1154 (2016).

[49] R. Lecourt, G. Linassier, G. Lavergne, Detailed characterisation of a swirled air/kerosene spray in reactive and non-reactive conditions downstream from an actual turbojet injection system, ASME 2011 Turbo Expo: Turbine Technical Conference and Exposition, American Society of Mechanical Engineers (2011), pp. 185–194.

[50] A. Briones, 2016, Private communication.

[51] A.W. Vreman, An eddy-viscosity subgrid-scale model for turbulent shear flow: algebraic theory and applications, Phys. Fluids 16 (10) (2004) 3670–3681.

[52] M. Bozkurt, M. Fikri, C. Schulz, Investigation of the kinetics of OH* and CH* chemiluminescence in hydrocarbon oxidation behind reflected shock waves, Appl. Phys. B 107 (3) (2012) 515–527.

[53] A. Giusti, E. Mastorakos, Detailed chemistry LES/CMC simulation of a swirling ethanol spray flame approaching blow-off, Proc. Combust. Inst. 36 (2017) 2625–2632.

[54] A. Stagni, L. Esclapez, P. Govindaraju, A. Cuoci, T. Faravelli, M. Ihme, The role of preferential evaporation on the ignition of multicomponent fuels in a homogeneous spray/air mixture, Proc. Combust. Inst. 36 (2017) 2483–2491.

[55] C. Coronado, J. Carvalho, J. Andrade, E. Cortez, F. Carvalho, J. Santos, A. Mendiburu, Flammability limits: a review with emphasis on ethanol for aeronautical applications and description of the experimental procedure, J. Hazard. Mater. 241 (2012) 32–54.

[56] C.L. Yaws, C. Gabbula, Yaws' handbook of thermodynamic and physical properties of chemical compounds, Knovel, 2003.

[57] K.M. Watson, Prediction of critical temperatures and heats of vaporization, Ind. Eng. Chem. 23 (4) (1931) 360–364.